Anatomy of thermal unrest at a hydrothermal system: Case study of the 2021-2022 crisis at Vulcano

Sophie Pailot - Bonnétat (✉ sophie.pailot@orange.fr)

   LMV: Laboratoire Magmas et Volcans   https://orcid.org/0000-0003-4653-2187

Victoria Rafflin

   LMV: Laboratoire Magmas et Volcans

Andrew Harris

   LMV: Laboratoire Magmas et Volcans

Iole Serena Diliberto

   Istituto Nazionale di Geofisica e Vulcanologia Sezione di Palermo

Gaetana Ganci

   Istituto Nazionale di Geofisica e Vulcanologia Sezione di Catania

Annalisa Cappello

   Istituto Nazionale di Geofisica e Vulcanologia Sezione di Catania

Guillaume Boudoire

   LMV: Laboratoire Magmas et Volcans

Guiseppe Bilotta

   Istituto Nazionale di Geofisica e Vulcanologia Sezione di Catania

Fausto Grassa

   Istituto Nazionale di Geofisica e Vulcanologia Sezione di Palermo

Alessandro Gattuso

   Istituto Nazionale di Geofisica e Vulcanologia Sezione di Palermo

Michael Ramsey

   University of Pittsburgh

Abstract

Hydrothermal systems can generate phreatic and/or phreatomagmatic explosions with little warning. Understanding the temporal and spatial evolution of geophysical and geochemical signals at hydrothermal systems is crucial for detecting precursors to unrest and to inform on hazard. Thermal signatures of such systems are poorly defined because data records are often too short or punctual compared to activity timescales, which can be decadal. La Fossa system of Vulcano has been monitored since the 1980s and entered a period of unrest in 2021.

We assessed the thermal signature using ground- and satellite-based data with temporal and spatial scales ranging from minutes to days. While continuously-recording stations provided continuous but point-based measurements, fumarole field vent surveys and ASTER and VIIRS images allowed lower temporal resolution but synoptic records to be built. By integrating this multi-resolution data set, precursory signals to the unrest could retrospectively be placed ranging from February to June 2021. Intensity of unrest increased during summer 2021, with an onset over a few days in September 2021. By September, seismic, CO_2, SO_2 and geochemical metrics also indicated unrest, leading Civil Protection to raise the alert level to yellow on October 1.

Heat flux, having been 4 MW in May 2019, peaked at 90 MW in September, and increased to 120 MW by March 2022. This ranked Vulcano as one of the highest intensity hydrothermal systems like Reykjanes, well ahead of Yellowstone and Nysiros We thus convolved our thermal data sets with all other monitoring data to validate a Vulcano Unrest Index (VUI) that can be potentially applied to any hydrothermal system.

The VUI highlighted four stages of unrest, none of which were clear in any single data set: baseline, precursory, onset and unrest. Onset was characterized by sudden release of fluids, likely caused by failure of sealed zones that had become pressurized during the precursory phase that began possibly as early as February 2021. Unrest has been ongoing for more than 18 months, and may continue for several more years. Our understanding of this system behavior has been due to hindsight, but demonstrates how multiparametric surveys can track and forecast unrest.

Introduction

Unrest at a hydrothermal system involves changes in the composition and flux of gas emissions, heightened heat flow, seismicity and/or deformation (e.g., Alparone et al., 2010; Capasso et al., 1997; Gambino & Guglielmino, 2008). Defining and tracking unrest at hydrothermal systems is fundamental for hazard assessment, as well as for understanding system dynamics and the association with explosive activity at "wet" volcanoes (Montanaro et al. 2022). Hydrothermal systems associated with non-eruptive, fumarolic degassing are liable to generate phreatic eruptions with little warning (e.g., Kato et al. 2015; Hamling 2017; Mayer et al. 2017), as well as phreatomagmatic eruptions which may have a long precursory period (e.g., Chouet and Matoza 2013; Geshi et al. 2016; Ardid et al. 2022).

Whether unrest leads to explosive activity or not, geophysical signals recorded for restless systems can provide insights into processes operation, in and above the hydrothermal system (Montalto 1994; Mannen et al. 2018; Moretti et al. 2020; Girona et al. 2021). In addition, even unrest that does not lead to explosive activity presents hazards as sometimes testified by high contents of toxic gases in the ambient air, as for example at Mammoth Mountain (USA) during 1989 (Sorey et al. 2000).

However, some metrics of unrest at such hydrothermal systems are poorly defined, and this includes the thermal signature. This is mostly because temperature surveillance at such systems is relatively recent, most time series to date being based on punctual, campaign-style approaches. As a result, continuous, high-temporal resolution thermal data sets recording the onset of unrest are lacking.

The ground temperature of a few points within the fumaroles field on the active cone of La Fossa, on the Island of Vulcano, has been monitored since 1984 (Diliberto 2011). In addition, surveys have been repeated annually since 1995 to detect changes of vent temperatures across the fumarole field (Harris and Maciejewski 2000; Harris et al. 2012), and ASTER and Landsat Thematic Mapper imagery have been used to constrain the thermal anomaly associated with the fumarolic activity and derive heat flux (Gaonac'h et al. 1994; Harris and Stevenson 1997; Silvestri et al. 2019; Mannini et al. 2019). Since January 2020 onwards, we have also been running up to five continuously recorded temperature sensor stations in and around the fumarole field. In parallel, we have

completed the fumarole temperature sampling at a frequency of up to three times a year, coupled with infrared camera imaging. Over the summer of 2021 Vulcano's hydrothermal system entered a new phase of unrest. This allows us to record and define the thermal signature of unrest, which is ongoing at the time of writing.

We thus use the unrest that began in the second half of 2021 to examine its surface effects across different thermal data sets, and detect how the temperature trends couple and decouple with other geochemical and geophysical data sets. This allows us to develop a model whereby unrest is heralded by a three-to-four months of increasing heat flow, before an impulsive onset of unrest over just one or two days.

Geological setting and context

Vulcano island is located in the southern part of the Eolian Archipelago (Fig. 1A) and is the emerged summit of a volcanic edifice that extends c. 1000 m b.s.l. (de Astis et al. 2013). It is a composite volcanic system built during a series of eruptive phases overlapping in time and space, with first activity being dated at 130 ka (Keller 1980; de Astis et al. 2013). The most recent activity has been focused to the north of the island at the currently active center of La Fossa cone and the Vulcanello peninsula (Fig. 1B) (de Astis et al. 2013; Fusillo et al. 2015). Structures and vents are aligned NNW-SSE, which is the same as the orientation of Lipari and Salina; an alignment which is controlled by the Tindari-Letojanni strike-slip fault system (Ventura 1994; Mazzuoli et al. 1995; de Astis et al. 2013). The associated NE-SW extensional stress field is linked to the two major calderas on the island, the Piano and the Fossa, which have been interpreted as pull-apart basins (Ventura 1994; Mazzuoli et al. 1995).

1) Historic activity

The Fossa, Faraglione and Vulcanello eruptive centers (Fig. 1B) have been active from 5.5 ka to present time (de Astis et al. 2013). The last eruption occurred in AD 1888–1890, and its description by Mercalli and Silvestri (1891) became the archetype for Vulcanian-type eruptions (Mercalli 1907). (Mercalli 1883) notes that emissions in late 1879 were sufficiently high that access to the crater was impossible for mining. De Fiore (1922) noted the establishment of a new fumarole field (maximum temperature 110°C) in the Fossa crater by 1913. Sicardi (1940) recorded increasing then decreasing temperatures between 1923 and 1937, with a maximum of 615°C in 1924 (de Fiore 1924). Another oscillation was recorded in the 1990s, with temperatures reaching a maximum of 690°C during 1992–1993 (Capasso et al. 1994; Chiodini and Cioni 1995). This thermal "crisis" coincided with an increase in the fumarole field area (Bukumirovic et al. 1997), and in the isotopic signature of gas emissions toward a clear magmatic component (Tedesco et al. 1991, 1995; Capasso et al. 1997). Since the late 1990s, the fumarole temperatures have generally decreased, with small variations being related to changes in near-surface permeability conditions and relocation of fumarolic activity rather than a magmatic source (Diliberto 2011, 2017; Harris et al. 2012).

2) Thermal character of the fumarole field

Heat flux at a fumarole field is partitioned between diffuse soil emissions and emission at the fumarole vents (Sekioka and Yuhara 1974; Chiodini et al. 2005; Harris 2013). At Vulcano the zone of fumarole vents is set within a broader zone of soil emission. The reducing conditions within the soil emission zone cause surfaces to be gray inside the heated zone, whereas soil emission zones are red (oxidized) beyond it (Fig. 1D). We here term the former the hot (grey) zone and the latter the cold (red) zone.

Chiodini et al. (2005) and Mannini et al. (2019) showed that heat flux from the zone of soil emission dominated the energy budget, accounting for 93 ± 2 % of the total flux, where total heat fluxes were in the range 5–13 MW between 2000 and 2019. However, although accounting for less than 8 % of the total flux, changes in the therma character (number and temperature) of the fumarole vents can give information on whether the system is in a phase of heating or cooling (Harris and Maciejewski 2000; Matsushima et al. 2003), as well as on localized changes in shallow system permeability conditions (Harris et al. 2012).

3) Hazard and risk

The Fossa cone eruptive activity is mainly explosive driven by phreatomagmatic processes (de Astis et al. 2013). Explosive activity is separated by periods of fumarolic activity, with there being four major explosive episodes between 1440 and 1890 (Biass et al. 2016). Considering past activity, eruptions of VEI 3 are considered the most likely to occur (Galderisi et al. 2013). Selva et al. (2020) made an extensive list of possible hazards on Vulcano island, ranging from eruptive hazards (tephra fallout, ballistic blocks and

bombs, pyroclastic density currents and lava flows) to non-eruptive hazards (hydrothermal activity and anomalies in aquifers, volcanic gases, volcanic flows and floods, landslides, tsunamis, seismicity). Vulcano Porto, is the municipality of the Island housing the majority of the tourist activity. During the peak of the tourist season, the island may house between 5,000 to 10,000 people (Galderisi et al. 2013), with Vulcano Porto and its hotels being located at the foot of the Fossa's western flank. The first buildings are within 400 m of the fumarole field. The proximity of the populated area to the potential eruption center makes it extremely vulnerable to any type of activity. As a result, the system as extremely well monitored, with continuous monitoring of fumarole and soil temperature beginning in 1984 (Diliberto 2011) and periodical samplings of the hydrothermal release to evaluate temporal changes in the magmatic contribution (Federico et al. 2010; Paonita et al. 2013)(Federico et al., 2022 submitted).

4) The new (2021 – present) phase of unrest

After around two decades of decreasing and relatively low levels of thermal activity (Harris et al. 2012; Mannini et al. 2019) a new period of unrest registered in monitoring data during summer 2021. CO_2, SO_2 fluxes and temperature data, from the INGV monitoring network, revealed slowly increasing emissions starting in June 2021, with a sharp increase in September 2021 (Inguaggiato et al. 2022a). The number of Very Long Period (VLP) seismic events and deformation signals increased starting September 2021 (Gangemi et al. 2022). The soil CO_2 flux in the Fossa crater reached levels of 34 000 g m^{-2} d^{-1} (Inguaggiato et al. 2022b), these being the highest values recorded since monitoring of soil gas emission began in 1989 (Carapezza and Diliberto 1993). As a result, Civil Protection raised the alert level from green to yellow on October 1, 2021 (Dipartimento della Protezione Civile 2021) and closed access to the Fossa cone on October 14 (Protezione Civile di Lipari 2021a, b). The Porto area was closed during night-time, due to health concerns related to increased CO_2 content in the air, and access to the island was forbidden to non-residents from November 20 (Protezione Civile di Lipari 2021d, c), following the deaths of small animals (cats and birds). In February 2022, monitoring variables began to stabilize, although at a much higher levels than prior to September 2021 (Inguaggiato et al. 2022a; Aiuppa et al. 2022). Thus, access to the island was re-opened on February 1 (il Mattino 2022), although access to the crater is still banned at the time of writing; and access to the beach fumaroles was closed in June 2022 (il Giornale di Lipari 2022).

Methods

During the period January 2020 to January 2022, we carried out six field missions, spaced by approximately three to eight months. We were able to thermally sample the system in January and October 2020, March, June and September 2021, and January 2022. This sampling frequency was limited by travel limitation and lockdowns due to the Covid pandemic. The full list of measurements and their locations during these field missions can be found in Appendix A.

1) Instruments

Ground-based thermal measurements

We used four different thermal instruments and five measurement strategies to define the various thermal surfaces, their relation to each other and their spatial distribution and temporal evolution. This involved different scales of measurements, which ranged from synoptic images of the whole area to detailed point-based measurements in-situ at representative zones. The point-based measurements could be extrapolated across each image and also provided ground-truth for the thermal imagery.

Three types of instruments were used to carry out the point-based measurements. K-type thermocouples were selected for the purpose of collecting punctual temperature measurements with a high accuracy. They were OMEGA's TJ1-CASS-M15U-600 and Ebro electronic thermocouples with a diameter of 1.5 mm and length of 600 mm, stainless steel sheath material and ungrounded junction because of the corrosive environment. The datalogger (DL) used had a 1.2 s response time. Dataloggers were also permanently installed in preferred areas of the crater (4-channel HOBO U12-008, weatherproof rugged enclosure, data storage of 43,000 measurements, and user detectable sampling rates 1 second to 18 hours). The permanently installed DL was connected to three TMC1-HD soil temperature sensors (operational range − 40°C to 100°C, accuracy of ± 0.25°C). The HOBO datalogger recorded measurements until the memory capacity was exhausted, which took around 90 days, using 3 channels and a 5-minute sampling rate. The data were downloaded manually and processed through the HOBOware Pro software before being exported to ASCII files. In addition, two thermal infrared (IR) thermometers were used for close distance measurements. The first one was a Fluke 568 Contact & Infrared Temp Gun, operating from − 40°C to 800°C (± 1.0°C or 1.0% of reading accuracy, whichever is greater). It has an

8–14 μm spectral response, 500 ms response time, with a distance-to-spot ratio of 50:1 and adjustable emissivity. When the Fluke 568 ceased functioning, it was replaced by another handheld gun-type thermometer: Extech OS-VIR50 operating from − 50°C to 2200°C (± 2.0°C or 1.0% of reading accuracy) and 150 ms response time. The infrared thermometer allows surface and vent measurements without environment disruption and with additional safety for the user. When used standing, the surface temperature measurement is made at a 0.5-1 m distance which equals to a measurement area diameter of 10–20 mm. It is possible to hold the trigger to generate maximum, minimum and mean temperature of a measurement series.

For a synoptic view, we used a tripod-mounted thermal infrared (TIR: 7.5–13 microns) camera, this been a FLIR SC660. This camera operates between − 40°C to + 1500°C in three ranges with a ± 1.0°C or 1.0% of reading accuracy. It has a 24°x18° field of view (FOV) with a spatial resolution of 0.65 mrad. The selected sampling rates ranged from 10 seconds to 1 minute and the 640 x 480 JPEG files were processed through the FLIR ResearchIR software.

Satellite-based thermal measurements

Two types of satellite infrared data were used. Firstly, the Advanced Spaceborne Thermal Emission and Reflection Radiometer (ASTER) aboard the spacecraft Terra is a partnership between NASA, Japan's Ministry of Economy, Trade and Industry (METI), the National Institute of Advanced Industrial Science and Technology (AIST) in Japan, and Japan Space Systems (J-spacesystems) (USGS 2022a). Terra's altitude is 705 km so that its ground track repeat cycle is 16 days (NASA Jet Propulsion Laboratory 2022). Its orbit is sun-synchronous, which means that at a particular latitude, it overpasses at the same time each day either during day (around 10 AM GMT) or night time (around 9 PM GMT). It offers high-resolution (15 to 90 m per pixel) images of the Earth in 14 different wavelength bands, ranging from visible to thermal infrared light, especially five TIR bands between 8 and 12 μm spectral range (TERRA 2022). In particular, it provides Level-2 products such as the Surface Kinetic Temperature (AST_08). AST_08 products are generated using the five TIR bands and deliver surface temperatures at 90 m spatial resolution for the land areas only. These temperatures are calculated by applying Planck's Law using the emissivity values from the Temperature/Emissivity Separation (TES) algorithm, which uses atmospherically corrected ASTER surface radiance TIR data (USGS 2022b). All ASTER products are freely available through Nasa's Earthdata Search platform (https://search.earthdata.nasa.gov/search) a few days after their collection.

Moreover, the Visible Infrared Imaging Radiometer Suite (VIIRS) sensor, on board Suomi National Polar-orbiting Partnership (Suomi NPP) and National Oceanic and Atmospheric Administration-20 (NOAA-20), was employed for the thermal monitoring of Vulcano. With a swath width of 3060 km in a near-circular, sun-synchronous, near-polar orbit, at 840 km mean altitude, VIIRS provides data every 12h, or less depending on the latitude, in 22 spectral bands from 412 nm to 12 μm of which: 5 (I-bands) at 375 m at Nadir, 16 (M-bands) at 750 m at Nadir and one day/night panchromatic band at 750 m spatial resolution throughout the scan respectively (Wolfe et al. 2013). Among these bands, the higher spatial resolution middle infrared band, I04 (centered at 3.74 μm) and the thermal infrared band I05 (centered at 11.45 μm) at 375 m are particularly useful for the monitoring of subtle thermal anomalies observable in closed conduit volcanos (Coppola et al. 2022). VIIRS archive imagery can be searched and downloaded via the NOAA CLASS Data web interface (https://www.avl.class.noaa.gov/) or automatically downloaded by using the wget utility via the Lance Near Real Time system, generally available within three-to-five hours from the satellite observation.

Gas Measurements

Soil CO_2 flux was measured using the accumulation chamber method (Chiodini et al. 1998). The field campaign of June 2021 was carried out using a West Systems composed of an A-type accumulation chamber (diameter 200 mm, height 100 mm) connected to a temperature-stabilized LI-COR LI-820 infrared sensor (0–20 000 ppm CO_2). The sensor has a detection limit of 1.5 ppm on CO_2 content and a 3 % accuracy on the reaing. Subsequent field campaigns were made by combining a West Systems C-type accumulation chamber (diameter 300 mm, height 100 mm) and a PP Systems EGM-5 (Environmental Gas Monitoring) infrared gas analyzer device, with temperature and pressure compensation. The EGM-5 device has a CO_2 range up to 50 000 ppm (5 %) and an accuracy of < 1 % over the calibratedrange.

2) Data collecting and processing

Surface temperatures (loggers)

Two HOBO datalogger temperature sensor stations separated by 50 m were installed in January 2020, west of the HTF fumarole field: RED_station and GRAY_station (Fig. 1C). The 50 m-profile (Profile1, Fig. 1C) between them crosses the transition between the "cold" zone, for which the ground surface is reddish-brown, and the "hot" zone, which is light grey (Fig. 1D). They record ground temperature (T_{15}, at 15 cm depth), surface temperature and air temperature (5 cm above ground level), the time interval between measures has been 5 or 10 minutes. Two temperature sensors with HOBO dataloggers (MZ1 and MZ2 stations) have been installed inside the hot zone, at the end of June 2021, the MZ1 station is about 25 m away from the most westerly middle zone agglomeration of vents. In addition, we used data from the permanent station maintained by INGV-PA which provides temperature at 15, 30, 45 and 60 cm depth (DDS station). This station is located on the east side of the HTF fumarole field, that is opposite to the HOBO loggers, and about 70 m away from the nearest fumarole.

Surface temperatures (TIR)

Ground surface temperature were collected using TIR thermometer. Harris and Maciejewski (2000) describe the main sources of error for infrared thermometer measurement as surface emissivity and atmospheric effects. The brightness temperature measurements need to be corrected for surface emissivity. This is a crucial point because surfaces inside the crater are different. We will mainly consider 3 types of surfaces here: (1) altered and reduced trachytic-rhyolitic material, light grey in color, (2) oxidized non-altered trachytic-rhyolitic material, reddish-brown in color, which both are deposits from the last eruptions, and lastly (3) sulfur deposits. Harris and Maciejewski (2000) used an emissivity of 0.9751 for trachytic-rhyolitic materials, 0.9089 for weathered sulfur surface and 0.8603 for fresh sulfur. New sample analyses (spectral analysis carried out by us using samples collected in May 2019) are consistent with these values, being respectively (1) 0.94445, (2) 0.9217, (3) 0.8858. Between the instrument and the target however, with a distance of 1 m, the fumaroles will emit vapor which contaminates the signal. To assess this effect, a comparison between thermocouple and TIR thermometer measurements was carried out inside the crater. A typical uncertainty of ± 1.0°C was found in windless conditions, which can increase up to ± 2.5°C in the presence of wind or cloud shadow. We always measured for a period of 10 to 20 seconds, a period much longer than the instrument response time.

At-depth temperatures (thermocouple)

During each survey, soil temperature was collected at a depth of 10 to 15 cm (T_{15}) on the west side of the fumarole field. It was done every 5 m on a 50 m-long line (Profile1, Fig. 1C), every 1 m on a 25 m² grid (Grid1, Fig. 1C), every 15 m on 250 m and 300 m long profiles (Profiles 2, 3 and 4, Fig. 1C). These measurements were performed through a narrow hole created using a 1 cm-wide chisel and a hammer. The thermocouple is immediately inserted into the hole. We always waited for the temperature reading to stabilize. Depending on surface temperature and steam presence, this could take between a few seconds to 2 to 5 minutes. In March and June 2021, we also made T_{15} measurements for every 5 m² cell in a 110*50 m grid called FA zone, centered on the middle zone (FA_grid, Fig. 1C). Once the crisis began, the measurements in the FA zone could not be made due to dangerous conditions. However, simultaneous measurements at the 25 m² grid in March and June allowed us to assess the representativeness of the smallest surveyed area (Grid1, Fig. 1C) to track the thermal effects of the unrest to the left of the FA zone, and out of high temperature fumaroles (HTF).

CO$_2$ accumulation chamber

Soil CO_2 flux (g m^{-2} d^{-1}) was processed with the "Flux Revision" software (https://www.westsystems.com/download/). Data processing uses the raw soil CO_2 content regression line measured by the instrument and ambient pressure-temperature (acquired from a Kestrel 5500 hand held weather station) to obtain the flux (ppm s^{-1}). Conversion in (g m^{-2} d^{-1}) is obtained by considering the volume and area of the accumulation chamber together with air temperature and pressure.

Fumarole surveys

Approximately each year since 1994, and since 2020 two to three times a year, a thermal survey using IR thermometers was conducted inside the fumarole field. The survey is always conducted following the same path and pattern to assure its statistical consistency. On the basis of historical evolution and thermal characteristics, the fumarole field was divided into five zones by Harris and Maciejewski (2000). These are: (1) the rim rifts which are two fissures that cut across the rim on the west of the field, (2) fumaroles in fractures aligned along the rim and, inside the crater, the (3) upper, (4) middle and (5) lower zones (Fig. 1D).

Thermal images

The thermal images were acquired during the day and night coincident with regular and scheduled ASTER overpasses (Ramsey 2016). On Vulcano, depending on the Daylight-Saving Time (DST), it is equivalent to a local time of 11 or 12AM for morning overpasses, and 10 or 11PM for evening overpasses. The tripod on which the camera is fixed is located opposite the fumarole field, on south rim of the crater (Fig. 1C). This position allows a synoptic view of the five fumarole zones from the rim to the bottom of the crater. It also gives an overview of the first platform level of the crater where the permanent dataloggers are placed and where the surface and at-depth temperature measurements are performed.

For each satellite overpass, acquisition started 15 minutes before and ended 15 minutes after the overpass, with a sampling rate of 1 image per minute. The sampling rate was increased to one image every 10 seconds two minutes either side of the scheduled overpass time. For a line-of-sight distance of 310 m to the bottom of the crater and 460 m to the rim, the pixel size ranged from 0.4 m to 0.6 m. To image the entire field, a panel of three images was taken as a panorama after the satellite overpass: NW, N, NE (Fig. 2). We selected for further processing the images with the most fume-free surface. Pixel temperatures were exported from the software ResearchIR using polygons, to avoid duplicating overlapping areas between images. The three frequency distributions were merged to allow a statistical analysis of the entire zone of fumarolic activity and soil degassing.

ASTER processing

Considering we only wanted to use easily accessible and ready-to-use data for fast response, only nighttime scenes were selected to avoid solar heating and thermal inertia effects. Furthermore, surface temperatures in the AST_08 image products are automatically corrected for emissivity and atmospheric effects. The scenes were loaded into ENVI (32 bits) as Thermal ASTER files to access their georeferencing data. The scenes were then exported into an ArcGIS geodatabase. Masking allowed extraction of temperature data for each pixel in two regions of interest (ROI): the Fossa crater, where the hotspot is visible, and Vulcanello, a cone north of the Fossa which currently has no anomalous heat and gas release (Fig. 1B). Maximum and mean temperatures from the ambient control (Vulcanello) were compared to those of the active target (i.e., the Fossa).

Within the Fossa ROI, the number of anomalous pixels was calculated using the temperature distribution (Appendix B). Almost all the distributions are bimodal: the first mode was interpreted as the background temperature distribution and the second mode as the anomaly (Fig. 3a). The number of pixels within the second mode was extracted and multiplied by the pixel area to obtain the thermal anomaly area (Fig. 3b, Appendix C).

Conversion to heat flow

ASTER and thermal camera images were used to calculate total heat flux as the sum of radiative and convective fluxes. Following Sekioka and Yuhara (1974) and Matsushima et al. (2003), radiative (M_{rad}) and convective (M_{conv}) heat fluxes were calculated on pixel-by-pixel basis, as follows:

$$M_{rad} = \sigma\epsilon(T_a^4 - T_b^4)$$

1

$$M_{conv} = h_c(T_a - T_b)$$

2

where, σ is the Stefan-Boltzman constant, ε is emissivity, h_c is the heat transfer coefficient, T_a is the temperature of the anomalous pixel, T_b the background temperature. Multiplying by pixel area converts these values from flux densities (M in W m^{-2}) to heat fluxes (Φ in J s^{-1}). This follows the definition of radiative terms given by Suits et al. (1975), but Q can also be termed heat flow (Harvey et al. 2015). For emissivity, we used the mean of our measured values and for h_c, we used 24 J K^{-1} from Sekioka and Yuhara (1974) and Matsushima et al. (2003). For the background temperatures, we used the minimum and mean temperatures of non-anomalous pixels. Values were summed for all pixels to obtain total Φ_{rad} and Φ_{conv} and the totals were added to obtain total heat flux [$\Phi_{tot} = \Phi_{rad} + \Phi_{conv}$].

VIIRS processing

VIIRS data were analyzed using a specialized version of CL-HOTSAT (Ganci et al. 2016) to measure the fumarole extension and temperatures in Vulcano in order to track temporal changes. CL-HOTSAT is a satellite data processing system used both for the near-real-time monitoring of high-temperature volcanic features (Rogic et al. 2019; Ganci et al. 2023) and for the extraction of the input parameters of numerical models used for lava flow hazard and risk assessment (Cappello et al. 2016; Zuccarello et al. 2022). The VIIRS data were downloaded as Level 1 Sensor Data Record (SDR) format including L1B calibrated radiance products VNP02IMG and VJ102IMG, for SNPP and JPSS-1/NOAA20 platforms respectively, and VNP03IMG and VJ103IMG VIIRS L1 terrain-corrected geolocation products containing the derived line-of-sight (LOS) vectors for each of the 375-m image-resolution or I-bands. The geolocation product was used for reprojecting and georeferencing the calibrated radiances that were then corrected for the atmospheric effect. Nighttime images were selected to avoid possible effects due to solar reflection. Moreover, in order to locate the thermally anomalous pixels a new hotspot detection algorithm was developed based on the Normalized Thermal Index (NTI) computed using the I4 and I5 bands (Wright et al. 2002).

$$NTI = \frac{I04 - I05}{I04 + I05}$$

3

This hotspot algorithm is a contextual algorithm in CL-HOTSAT where the volcanic area includes the whole La Fossa crater area and the non-volcanic area the rest of the island. We flag a pixel in the volcanic area as a hotspot if its value for NTI (NTIHS) is greater than the normal variation of NTI in a non-volcanic area (NTINVA) according to:

$$NTIHS > Mean_{NTINVA} + 3 * SD_{NTINVA}$$

4

For each pixel flagged as a hotspot the radiant heat flux is computed by assuming the pixel as composed by two thermal components. A dual band technique is then applied to the hotspot pixel in order to infer their thermal structures and the Stefan-Boltzmann law is applied to compute the associated radiant heat flux.

Results

1) Punctual measurements of temperature and soil CO_2 flux

Measurements of T_{15} were made at exactly the same locations every 5 m along the 50 m-long Profile1 during every survey (Fig. 1C). The profile crosses the transition between the cold zone and the hot zone. Since 2020, the location of this transition has been stable and located at the 20 m mark (Fig. 4). Between January 2020 and March 2021, T_{15} for the cold zone was stable, varying by no more than 3°C. Profile1 had been visited annually since 2015, and this stability in position of transition and T_{15} level is apparent in all surveys (Appendix D). Until June 2021, the transition was marked by an increase in T_{15} by 3 to 10°C, with temperatures up to 20°C higher than the cold zone, and occasionally hot spots of 80 to 90°C after the transition. These hotspots were highly localized, but spatially and temporarily variable. From January 2020 to June 2021 a persistent hotspot was detected on the 25 m mark. However, in September 2021, the hotspot expanded to include the entire hot segment of the line. At the same time the hot-cold transition moved 5 m into the cold zone, with temperatures at the 20 m mark increasing from 25°C in January 2020 to 90°C in September 2021. By January 2022, the 20 m mark temperature had decreased by 40°C as had the extent of the hotspot. However, T_{15} levels and the size of the anomaly remained higher than before June 2021. The limit of the hot zone remained stable at the 20 m mark through May 2022. This all implies an expansion of the hot zone, as well as enhanced heating of the hot zone from June 2021 onwards.

In March 2021, T_{15} for Grid1 was between 30 and 40°C with a hotspot (T_{15} = 60°C) in the NE corner, and a subtler hotspot (at 46°C) in the SE corner (Fig. 5a). In June 2021, hotspots were located in the same two locations, but the SE hotspot was more apparent and the whole area had heated by 20°C (Fig. 5b). By this time, temperatures at the hotspots had reached boiling point temperatures. In September 2021, almost the whole area was at boiling point (Fig. 5c). By January 2022, boiling point temperatures had focused in a NE-SW diagonal zone around which temperatures were 50 to 60°C (Fig. 5d). This zone was already apparent in the September

grid (Fig. 5c) and persisted through May 2022 (Fig. 5e), as did a hot spot to the NW. The linear feature likely represents a line of preferential fluid circulation, such as a buried fracture.

Temperature distributions across the FA grid (Fig. 6, surface = 5500 m2) showed a similar behavior between March and June 2021. In this area we measured an extensive increase in T_{15}, to values close to boiling point. Since the behavior and level of temperatures have been similar between the FA grid and Grid1, we avoided the higher risk of repeatedly accessing the FA grid and trust that the last is representative of the behavior of the most extended hot zone. The FA grid showed the alignment of hot temperatures along the break-in slope at the top of the inner crater. Grid1, even at a minor scale, highlights a prominent NE-SW alignment, which is the direction of the rim rifts and all regional structures as controlled by the extensional stress field associated with the Tindari-Letojanni fault system (Ventura 1994; Mazzuoli et al. 1995).

Soil CO_2 flux was measured at the same location as temperature along Profile1 to Profile4 and Grid1 (Fig. 1C). The increase in temperature is clearly linked to a collocated increase in CO_2 flux. On Grid1 for example, the average flux increased from 900 g m-² d-1 in June to 4522 g m-² d-1 by September. Figure 7 shows T_{15} and soil CO_2 flux on Profile2 in June and September 2021. Soil CO_2 flux peaks and hot spots are well correlated, indicating high permeability locations. However, the correlation is less where surface temperatures are closer to background. This effect is due to the low permeability where soil CO_2 flux is almost zero and temperatures are lower.

1. Fumarole field survey

Temperature data for the fumarole field as a whole show a general decline following the 1990s crisis (Fig. 8) to lowest levels recorded in March 2021. Thereafter there is an increase in the mean temperature which, 14 months recovered to levels higher than in 1994. The trend is the same in terms of number of fumaroles. The exception to these generalities is a peak in the mean temperature in 2018; a peak which is not apparent in the maximum temperature and number of fumaroles. This appears to be a spurious result from averaging the lowest number of fumaroles ever recorded (Fig. 8). To check and clean such anti-correlations we developed a thermal index (FTI), which is:

$$FTI = \frac{(T_{max} * T_{mean} * Nb_v)}{SD^2 * 10^4}$$

5

where T_{max} and T_{mean} are the maximum and mean temperatures for each survey, and SD is the standard deviation and Nb_v is the number of vents measured. This index is designed to use T_{max} as a proxy for the absolute thermal state of the fumarole field, T_{mean} for the total heat flux, Nb_v for the size of the fumarole field and standard deviation for the thermal behavior, where small standard deviation has been shown to be associated with cooler periods, and high standard deviation with heating periods (Harris and Maciejewski 2000).

This cleans out the trend showing a general decline through 2021, with a recovery to around the 1996 levels by June 2022 (Fig. 9). This approach minimizes the influence on the thermal characteristics of the permeability crises. During such crises, heat flux increases due to increased fracturing and fluid flow without any change in magmatic input, as occurred between 2002 and 2010 (Harris et al. 2012). It also confirms the current trend as not being related to such a process. If we look at the temperature data and index zone by zone, we see the same trend in reactivation since June 2021 across all zones (Appendix E). This system reactivation is supported by field evidence, where we observed (1) establishment of fissures with low temperature fumaroles outside of the main fumarole field area, (2) increase presence of high temperature sulfur mineralization (liquid orange sulfur and black sublimates), (3) eruption of sulfur flows and sulfur pyroclasts (Fig. 10), (4) increase deposition of yellow sulfur and (5) melting of the sulfur component of the substrate to leave a fine-grained grey silicate powder (Harris and Maciejewski 2000).

3) In-situ temperature in the hot zone

The behavior of local temperature recorded at GRAY station, showed over 1 year in 2020 a negligible temperature differential between shallow ground and shallow air temperature, thus suggesting a robust local background reference (ΔT ± 1°C, Fig. 11). The

positive differential values, recorded from April 2021 gives instead a measure of the thermal anomaly affecting the ground surface, since the very beginning of the unrest period, and it reflects the preparation phase of internal heating (positive differential values ΔT > 2−3°C in April 2021, reaching 8°C by the end of 2021, Fig. 11). The temperature differential is evaluated by the equation:

$$\Delta T = T_h - T_0$$

6

T_h being the average daily temperature of the internally heated surface and T_0 being the average daily ambient background temperature, monitored for 2 years.

At depth of 0.15 m, rainfall causes the major external perturbation on ground temperature. Rainfall events cause soil temperature to decrease by up to 20°C, with this section of ground needing from one day to two weeks to recover the previous unperturbed temperature values (Fig. 12). However, around these events we see a systematic increase in T_{15} by 0.167°C per day until August 23 on MZ1 station, at which point the rate increased to 0.7°C per day to mid-September. Thereafter we record three pulses which reach boiling temperature. The three pulses had durations of around half a month, were centered on late-September, late-October and late-November, and were separated by half a month, giving a one-month cycle. Both later pulses were marked by discrete peaks with maximum temperature up to 110°C. The time series collected at GRAY and to a lesser extent DDS station mimic the behavior of MZ1, with lower temperature values and less marked pulses and peaks (Fig. 12). This is consistent with DDS being further from the fumarolic zone, where the difference in temperature and response at the two stations suggests higher permeability conditions at MZ1. However, there is a temperature pulse centered on the beginning of January at GRAY that is not found at MZ1.

4) Thermal camera images

Thermal images were collected on 25 June and 29 September 2021 (Fig. 13), during nighttime satellite overpasses. These images showed expansion of the thermally anomalous area, especially in the west and south-west sectors of the crater, where the anomaly spreads into previously cold zones. It also shows reactivation of areas within the fumarole field, especially along the rim rifts, and in the upper zone and areas of the middle zone.

Pixel temperature frequency distributions for the two images are given in Fig. 14a. Both distributions are right-skewed, but the distribution for September has a more robust high temperature tail (Fig. 14a). This results in a lower skewness and highly positive kurtosis for September, indicating heating (Harris et al. 2009). The September distribution can be separated into three populations: (1) background temperatures (normal distribution), (2) heated ground (normal distribution), and (3) pixels containing fumaroles and subsequent heated ground (Fig. 14c). The skewness from June images is higher because background temperatures dominate more than in September images (Fig. 14b; Table 1). Differently from September, in June the background and the (steam) heated populations can be distinguished just on the base of the surface temperature.

Table 1
Temperature statistics for the camera thermal images

	Maximum	STD	Skewness	Kurtosis
June 2021	116	4.7	2.0	7.2
Sept 2021	150	7.3	1.9	11.9

5) Satellite images

Since we did not find a significant correlation between the temporal variation of mean or max surface temperatures and the number of anomalous pixels (Appendix F), we developed a two-step process to highlight the thermal anomaly and isolate any temporal trends.

The first step isolates the thermal anomaly by using an ambient control to define ΔT_{max}:

$$\Delta T_{max} = Tmax_{crater} - Tmax_{control}$$

7

where $Tmax_{crater}$ is the maximum temperature from the anomaly in the Fossa crater area and $Tmax_{control}$ is the maximum temperature of the ambient control area on Vulcanello (Fig. 1B). T_{max} on Vulcanello is highly variable in space and time, but it does not correlate with the background around the thermal anomaly of the active cone. However, this index does not consider any trend related to the number of anomalous pixels (Fig. 15a).

Thus, the second step combined a statistical-based thermal approach with the number of anomalous pixels to create the Satellite Thermal Index (STI) of each usable ASTER scene:

$$STI = \frac{Tmax_{crater} * Tmean_{crater} * SD_{crater} * Nb_p}{Tmax_{control} * Tmean_{control} * SD_{control}}$$

8

where $Tmean_{crater}$ is the average temperature from the anomaly, $Tmean_{control}$ is the average temperature of the ambient control area on Vulcanello, SD_{crater} is the standard deviation for the anomalous temperature distribution, $SD_{control}$ is the standard deviation on Vulcanello and Nb_p is the number of anomalous pixels. The role of the numerator is similar to that of Eq. 3 so that we divide by $Tmax_{control}$ to minimize the influence of seasonal and diurnal cycles. The index values are underestimated in case of partial cloud cover or rain fall (such as the mid-July 2021 storm event) (Fig. 15). We now see an increase of STI possibly beginning in mid-May over the baseline, to reach a first peak at the end of September 2021 (which might be underestimated because of the partial cloudiness); this is coherent with the increase of anomalous pixels, which also exceed the baseline in mid-May; thereafter the STI remains at a high level (Fig. 15). The time variations of STI in Fig. 15 mimics the temperature data directly measured by contact sensors in the hot zones (Fig. 12).

6) Cross validation of heat fluxes (VIIRS ASTER ground-based comparison)

ASTER derived radiative heat fluxes show typical values of 4–8 MW until July 2021. Thereafter they increase to a different range (8–20 MW, Fig. 16a). Due to differences in surface types, altitude, vegetation cover and slope aspect, we decided to use hot spot proximal background characterization from within the Fossa ROI instead of using Vulcanello in our heat flux background calculations. The VIIRS derived radiative heat fluxes result in a set of retrieved values more scattered than ASTER's, because of pixel size is greater (375 m) and the subpixel cloud contamination. At the same time, VIIRS derived radiative heat fluxes generally remain within the boundaries of ASTER estimations and even show a comparable trend (Fig. 16a). Thermal camera derived heat fluxes are lower, being 1 to 2 MW (Fig. 16a). These estimations are consistent with the VIIRS derived radiative heat flux obtained by Coppola et al. (2022) i.e. 1.2 MW, with theirs values targeting only the fumarole field. This means that in terms of radiative heat flux the fumarole field contributes to 5 to 10 % of the cone-wide fux (Mannini et al. 2019). Actually, the ground based thermal camera only targets the fumarole field on the NE inner flank, whereas ASTER and VIIRS target the cone-wide heat flux (the entire crater and all flanks).

In terms of total heat flux, ASTER remote sensing supplied variable levels: between 30 and 60 MW until October 2021, with a possible ramp up beginning in June, heat flux increased abruptly to 80–90 MW From October 2021 with a peak at 120 MW in March 2022 (Fig. 16b). These values are higher than those calculated in 1998, which is the end of the previous thermal crisis measured on the active cone, which were of the order of 21 MW (Chiodini et al. 2005). These total heat fluxes are also higher than the pre-crisis baseline of 5 to 14 MW from Mannini et al. (2019), for the period from 2000 to 2015. The total heat fluxes evaluated by the ground based thermal imagery are 18 to 32 MW (Fig. 16b), likewise increasing from July. Note that the thermal camera measurements target the NE inner flank only. The percentage contribution of this zone to the total heat flux decreased through time (Fig. 16b), and it is consistent with spreading of the thermal zones and of degassing chimneys onto the outer flanks and well beyond the crater. Also the stressed and dead vegetation (Fig. 17) on the north rim (around the Forgia Vecchia crater, Fig. 1b) and on the south rim is consistent with increased soil heating and diffusive CO_2 degassing.

Discussion

1) Gas and Heat flux partitioning

There is no apparent correlation between T_{15} and soil CO_2 flux if we consider the entire data set (Fig. 18). One possible explanation for lack of correlation is that it is hard to seal a high-volume accumulation chamber on a rough and hard ground surface, so the gas emission (in this case CO_2) can escape around the edges of the chamber. Under such a condition, a variable portion of the flux will not reach the gas detector. However, the primary cause is likely due to the case-hardened crust (cf. Malin et al. 1983) produced by the alteration of hydrothermal salts. Very local low permeability of such surface crusts hinders CO_2 escape, and causes gas to flow laterally to more permeable zones. At the same time the hardened crust will have a higher thermal conductivity than a granular material and is more efficient at transferring heat from the hot fluids arriving beneath the crust to the surface (see Tables in Clark 1966). Hot spots thus have a better correlation with peaks in soil CO_2 flux, although we find dislocation between preferred emission points at a meter scale (Fig. 7), hindering spatial correlation. This is especially true for measurements made within one meter of each other, as for example at Grid 1, where data are highly scattered and uncorrelated (Fig. 18a). Instead, measurements separated by several meters smooth out such dislocation, reducing scatter and improving correlation (Fig. 18b). The correlation is better for Profile 1 in September (R^2 = 0.80) than in June (R^2 = 0.73) (Fig. 18b) because the number of hot spots increased (Fig. 7). Figure 18 thus reveals widespread heating and increased soil CO_2 flux over the 3-month period between June and September 2021.

2) Soil temperature pulses

A link between increased temperatures at HT fumaroles and volcano-seismic long-period events (LP) was already observed at Vulcano, by Alparone et al. (2010) and Cannata et al. (2012) between 2004 and 2007. In particular, they noticed a sharp increase of both seismicity and temperature in 2007, which they called an "impulsive onset". Three referenced hypotheses, originated from different sources, can explain this phenomenon: (1) an external cause, like rainfall, inducing perturbations of the hydrothermal system (Nakano and Kumagai 2005), (2) a transient permeability increase leading to upward migration of hydrothermal fluids (Harris et al. 2012), and/or (3) increased release of hot gases from the deep magma body, leading to heating and drying of the hydrothermal system (Alparone et al. 2010; Cannata et al. 2012).

The first two temperature pulses of late-September and late-October 2021 respectively coincide with the first two Very Long Period (VLP) swarms (Fig. 12). Whereas, the last temperature pulse at MZ1 in late-November is not associated with any VLP events, and the fifth VLP swarm in mid-December is followed by a temperature peak at GRAY (Fig. 12).

The previous VLP events registered at Vulcano's hydrothermal system have been interpretated as being linked to increases in the gas volume fraction in the fluid, sudden release of pressured gas, and generation of small cracks (Alparone et al. 2010; Cannata et al. 2012). In such case, fluid pressure increases to exceed the mechanical resistance of any obstruction inside hydrothermal fluid-filled cracks (= increased fracturing). The fluid flow then resonates inside the newly opened cracks (= increase of fluid flow) (Alparone et al. 2010).

Moreover, rainfall events in our data do not appear systematically relate to VLP swarms (Fig. 12): In particular, a very intense rainfall event in July was not associated with any VLP events. Whereas, the first VLP events in September occurred a few days after the first rain since July. This could be interpreted as a water influx which finalized the destabilization of an already charging and unstable system. Although in absence of other evidences, it also might have been a simple coincidence. This is not the case, because the interpretation of gas geochemistry variation, observed between October and December 2021, in the fumarolic emission accounts for the release of predominantly magma-derived fluids (Aiuppa et al. 2022). The increased release of hot gases from the deep magma body (hypothesis 3) is therefore the most likely explanation supporting the direct relationship between temperature and VLP swarms during this unrest period, with an external cause (hypothesis 1, of the intense rainfall as a triggering) possibly explaining the onset of the VLP seismicity.

The depth of the VLP events at Vulcano has been estimated to be between 0.5 to 1.1 km b.s.l. by (Alparone et al. (2010). This is in agreement with depths of 0.6 to 1.2 km b.s.l. found by (Gangemi et al. (2022) in September-October 2021. The synchronicity between the VLP swarms and peaks in T_{15} at the periphery of the fumarole field suggests that fluids released from depth contributed to near-immediate surface heating above a highly permeable medium during September and October 2021. In this case the heat flux was widely distributed, rather than being channelized by primary fractures feeding high temperature fumaroles. We note the same effect in the T_{15} profiles in September, when most of the line was still displaying heating conditions, although the temperature of a fumarole mid-way along the line decreases slightly (Fig. 7c).

In December, HTF temperatures plateaued at a maximum of 360°C (Fig. 19), implying channelization towards the high temperature fumaroles. Simultaneously, the surface temperature response of the VLP swarm was only reflected at GRAY and lagged by roughly two weeks. We interpret this as being due to less efficient heat transfer to the surface at our stations across a less permeable medium. This could imply that localized self-sealing and clogging of the very-shallow fumarolic system in a relatively short timescale (Stix and de Moor 2018; Montanaro et al. 2022; Ardid et al. 2022) had already begun at the system periphery. The increased fluid flow into the newly opened pore and/or micro-fractures after the first outbreak could have increased alteration of the host rock as well as sulfur and silica mineralization (Gurioli et al. 2012; Sutawidjaja et al. 2013; Heap et al. 2019; Mick et al. 2021). Indeed, sulfur viscosity increases drastically above 160°C (Scolamacchia and Cronin 2016), so that fracture/pore sealing and subsequent loss of permeability could occur at shallow depth in the multilayered hydrothermal system (Christenson et al. 2010; Sutawidjaja et al. 2013). The onset of sealing and channelization thus could have developed locally over the timescale of a few (4 ± 2) weeks (Fig. 12, Fig. 19).

3) Heat flux partitioning

Between February 2021 and March 2022, the partitioning between convective and radiative flux remains stationary because the heated surface temperatures still remained well below the crossover point where radiation begins to exceed convection (250−400°C, Keszthelyi et al. (2003)). Figure 20 shows the stacked chart of the convective and radiative heat flux (RHF) calculated from ASTER images and an increase in heat flux beginning between the acquisition of scenes 8 and 10, i.e., during mid-June 2021.

4) Summary of the changes

A summary timeline of the evolution of all datasets considered is given in Fig. 20. Onset of unrest is clear in all data sets, but the time at which unrest becomes evident is variable, depending on which data set we consider. In hindsight, precursors to the unrest were found at the HTF, which began to increase in temperature as early as February 2021 (T3, Fig. 19). The outlet highest temperature on the other fumarole on the outer rim (T2, Fig. 19) began to increase only after June 2021. However, this trend was not apparent at the monitored fumaroles on the inner slope (FA), where temperatures remained stable throughout the period. The unrest was detected at GRAY during April, and possibly in the Satellite Thermal Index in late-May. Temperature increases during the summer are also detected in the diffuse degassing zones (DDZ), and by the FTI as well as the T_{15} line and Grid 1. The different sampling rate at these locations (every 3−4 months) limits temporal precision, however we can say that unrest began after our mid-June field campaign.

An increasing trend in soil CO_2 flux began in mid-2020. However, baseline levels were not exceeded until mid-June 2021 (Inguaggiato et al. 2022b). SO_2 flux began increasing in April 2021, exceeding the baseline sporadically in June, and persistently from August 2021 onwards (Inguaggiato et al. 2022b). VLP events increased from zero to several hundred events per day during September (Gangemi et al. 2022), at which time increasing trends in all thermal and CO_2 metrics also picked up (Inguaggiato et al. 2022b). The geochemistry of the gas sampled from fumaroles indicates an increasingly dominant magmatic signature from July 21 onwards (Aiuppa et al. 2022; Inguaggiato et al. 2022b).

The start of the seismic events in early September indicates the breaking of the system seal, when fluids could ascend to the surface easier, thus explaining the increase of all signals from this point onwards.

On the basis of these trends, we used seven parameters (n), including two thermal parameters from this study and five from the monitoring network, to create a Vulcano Unrest Index (VUI). The four terms (x) of the equation are normalized using their minimum and maximum values registered during 2021:

$$N_x = \frac{x_{(t)} - x_{min}}{x_{max} - x_{min}}$$

9

Then,

$$VUI = \frac{N_T + N_{G1} + N_{G2} + N_S}{4}$$

10

With,

$$T = \left(\overline{m_{T2}} + \overline{m_{T3}} + \overline{m_{GRAY}}\right) * \overline{m_{STI}}, G1 = \overline{m_{CO_2}}, G2 = \overline{m_{SO_2}} \, and \, S = \overline{m_{VLP}}$$

11

Here, $\overline{m_n}$ is the monthly average value of parameter n. We use the monthly averaged values for T2 and T3 (Fig. 19); the monthly averaged difference between surface and air temperatures at GRAY; and the monthly averaged values of STI. We combine the thermal parameters with monthly averaged values of soil CO_2 and SO_2 flux from Inguaggiato et al. (2022b) and the monthly sum of VLP events from weekly bulletins of INGV (Istituto Nazionale Di Geofisica e Vulcanologia 2021b, a). Values used are given in Table 2. Although initialized with the monitoring data from the active cone of La Fossa (Vulcano island), the VUI is an index is designed and tested for potential use at any hydrothermal system entering unrest, where similar monitoring data sets are available.

Table 2
Parameters used to calculate VUI

	T3 (°C)	T2 (°C)	Soil CO_2 flux (g m^{-2} d^{-1})	SO_2 flux (t d^{-1})	VLP	STI	GRAY (°C)	VUI
Jan-21	171	256	891	21	13	*20*	0.9	0.008
Feb-21	175	250	953	21	10	20	0.3	0.008
Mar-21	204	262	2009	20	7	34	0.4	0.031
Apr-21	203	267	1222	20	6	29	1.8	0.014
May-21	223	264	932	20	4	54	2.3	0.025
Jun-21	247	265	973	31	2	77	3.5	0.073
Jul-21	277	272	3148	26	0	63	3.1	0.089
Aug-21	300	281	4618	34	0	123	3.9	0.184
Sep-21	331	294	12115	63	625	291	3.2	0.760
Oct-21	361	322	15553	107	695	*300*	3.5	1.000
Nov-21	366	351	14124	100	36	*200*	4.6	0.640
Dec-21	373	361	10024	101	608	161	5.1	0.747

Parameters from left to right: monthly average temperature of fumaroles T2 and T3 (Fig. 19), monthly average soil CO_2 flux and SO_2 flux (Inguaggiato et al., 2022b), monthly sum of VLP events (Instituto Nazionale Di Geofisica e Vulcanologia, 2021b, 2021a), STI and monthly average of surface temperature minus air temperature at GRAY station. The parameters generated in the course of this study are bold. STI's value in italics are estimates to fill in the gaps in ASTER images.

The VUI has been plotted in Fig. 22 to tracking and describing unrest levels, based on very different monitoring data independently acquired for surveillance of volcanic activity. The VUI indicates four periods (Fig. 22): (1) background levels with VUI < 0.02 until May 2021, (2) a precursory period through mid-August, when VUI systematically increased to 0.2, (3) the onset between mid-August and mid-October, when the VUI increased to a peak of 1, before declining (4), but remaining high (> 0.6) through the end of the year 2021.

5) Thermal crisis model

We propose a model for the onset of unrest, by interpreting the sequence of surface thermal effects as summarized in Fig. 23. This involves the following four steps.

1. Onset of the thermal crisis was triggered by injections of magmatic fluids into the shallow hydrothermal system. This occurred between January and June 2021, as indicated by the change in geochemistry of fumarole gas samples (Aiuppa et al. 2022) (Federico et al., submitted).
2. This caused an increase in heat ascent, which was recorded at the surface beginning in February 2021 at some monitored fumaroles, and in April 2021 at our soil temperature stations. Thermal anomalies intensified in ASTER data in mid-May (Fig. 15).
3. Initially, increased fluxes were focused in the heat chimney defined by self-sealing around the fractured conduit of heat and fluid ascent below the Fossa fumarole field, as was suggested by Harris and Maciejewski (2000). Enhanced heat fluxes began to spread into the periphery of the fumarole field during Spring 2021.
4. The impermeable seal surrounding the heat chimney failed early in September and was associated with seismic swarms, causing the area of thermal and gas emission to expand out of the pre-crisis borders. At the same time, fluid ascent became much more efficient so that heat and gas fluxes increased abruptly.

This 2021–2022 crisis contrasts with that of the 1990s, when expansion of the heated area was less marked, and tended to occur within a narrower zone interested by fumarolic activity (Bukumirovic et al. 1996, 1997). In addition, the 1990s crisis was characterized by a marked increase in maximum temperature (Capasso et al. 1994; Chiodini and Cioni 1995) whereas the 2021–2022 crisis was not. This suggests that the self-sealed heat chimney remained intact during the 1990s crisis so as to focus an increased flux across a smaller area; to be reflected in an increase in the maxima 690°C. Instead, failure of self-sealed zones in September 2021 caused expansion of the emission vents, resulting in a widespread, but less intense heating of the ground. Indeed, although CO_2 fluxes increased well above those of the 1990s, maximum temperatures remained around 380°C.

The increase in heat flow amounts to around 1060 MW km^{-2}, that is an order of magnitude higher than that calculated for Vulcano during the 1990s by Harvey et al. (2015), i.e., 193 MW km^{-2}. This increase in emission actually places the heat fluxes from the Vulcano Fossa among the highest from hydrothermal system on the planet, showing the same release as the highest hydrothermal flow that was evaluated in Reykjanes (Iceland) as 1048 MW km^{-2}, in the collation of Harvey et al. (2015). For what concerns Vulcano, the March 2022 heat flux of 120 MW compares with 21 MW calculated for the 1990s (Chiodini et al. 2005) and 5 to 14 MW between 2015–2018 (Mannini et al. 2019).

Conclusion

After two decades of relative quiescence, Vulcano entered a phase of unrest in late summer 2021 following a four to five month-long period of precursory signals. Precursory signals are mostly marked by increased heat and fluid flow to cause temperatures, gas fluxes and compositions to change. Unrest was characterized by an acceleration of thermal and gas parameters, as well as the onset of seismicity and deformation. We show here how ground- and satellite-based thermal parameters can be used to track and characterize evolutive phases from baseline hydrothermal release through the onset of unrest. We combined these with geochemical and geophysical parameters, to fully characterize and explain various phases of unrest, especially the transition from a precursory condition. At the time of writing (February 2023), unrest had been continuing for 18 months with no explosive activity. The previous phases of unrest continued for four to five years before activity returned to baseline levels over a similar period. The last eruption of Vulcano (1888–1890) was also preceded by a few years of unrest. Thus, unrest at Vulcano may or may not end in eruption. The main difference between the current unrest and that of the 1990s is that a much higher heat and gas flux has been emitted over a much greater area. This was due to failure of self-sealed zones in September 2021, which did not appear to happen in the 1990s when an increased heat flux instead remained channelized in the self-sealed chimney.

At Vulcano, unrest has been previously explained by a plumbing system model where multiple compositionally-distinct and stationary reservoirs at different depths provide fluids which ascend to a roof zone (Paonita et al. 2013). Paonita et al. (2013) suggest that the unrest of 2021 was triggered by failure of the impermeable roof above a building gas "bubble" to abruptly release fluids into the hydrothermal system. Aiuppa et al. (2022) explained the SO_2 degassing during October-December 2021 by the presence at a depth of 4–5 km of a relatively small volume (~ 3×106 m3) of mafic magma. We see the building phase by subtle

increases in heat and gas flux and the roof failure by an abrupt acceleration of these fluxes. Continued high soil temperature and CO_2 flux through the time of writing suggest that fluid and heat fluxes from deep remain elevated. Given the duration of previous unrest at Vulcano, this may continue for several more years. The question is: will the unrest end passively or explosively, and when?

Because the timescale of unrest has been decadal, our data capability has to date not properly recorded a full cycle of it. As a result, our understanding of the 2021–2022 phase has only been possible with hindsight. In the future, it may be possible to use trends and interpretations given here to track such an event. However, we still have to collect data for the completion of this unrest and only at that point, we will be able to adequately completely track a full cycle of unrest at Vulcano's hydrothermal system. In the meanwhile, we hope that the results from this multiscale thermal approach, completed by a multiparameter data comparison, will be useful for interpreting other evolving thermal condition based on remote sensing of the less monitored hydrothermal and volcanic system around the world.

Abbreviations

ASTER: Advanced Spaceborne Thermal Emission and Reflection Radiometer

b.s.l.: below sea level

DL: Datalogger

EGM: Environmental Gas Monitoring

FOV: Field OF View

FTI: Fumarole Thermal Index

HTF: High Temperature Fumaroles

IR: Infrared

LOS: Line Of Sight

NTI: Normalized Thermal Index

RHF: Radiative Heat Flux

ROI: Region Of Interest

SD: Standard deviation

STI: Satellite Thermal Index

T_{15}: ground temperature at 15-cm depth

TIR: Thermal Infrared

VEI: Volcanic Explosivity Index

VIIRS: Visible Infrared Imaging Radiometer Suite

VLP: Very Long Period

VUI: Vulcano Unrest Index

Declarations

The authors *must* provide the following sections under the heading "Declarations".

Ethics approval and consent to participate

Not applicable

Consent for publication

Not applicable

Availability of data and materials

The datasets used during the current study are available from Sophie Pailot – Bonnétat on reasonable request.

Competing interests

We declare no competing interests

Authors' contributions

SPB contributed to the conception and design of the project, acquisition, analysis and interpretation of the data, and wrote the original draft of the work.

VF contributed to the acquisition, analysis and interpretation of the data and participated in the writing of the draft

AH contributed to the conception and design of the project, acquisition and interpretation of the data, participated in the the original draft of the work and substantial revisions.

ISD contributed to the acquisition and interpretation of the data and made substantial revisions

GG contributed to the acquisition, analysis and interpretation of the data, participated in the writing of the draft and made substantial revisions

AC contributed to the acquisition, analysis and interpretation of the data and participated in the writing of the draft

GBillota contributed to acquisition and analysis of the data with software processing

GBoudoire contributed to the acquisition, analysis and interpretation of the data and made substantial revisions

AG contributed to the acquisition and analysis of the data

FG contributed to the acquisition, analysis of the data

MR contributed to the conception of the project and made revisions

not have been possible without the help and support of Tanino at the Casa Genovese (Vulcano), Maurizio at "La Forgia" (Vulcano), Manfreddi at La Giarra (Vulcano), all at the Filadelfia (Lipari), "Faraglione" bar and the Carabinieri of both Vulcano and Lipari."

References

1. Aiuppa A, Bitetto M, Calabrese S et al (2022) Mafic magma feeds degassing unrest at Vulcano Island, Italy. Commun Earth Environ. https://doi.org/10.1038/s43247-022-00589-1. 3:

2. Alparone S, Cannata A, Gambino S et al (2010) Time-space variation of volcano-seismic events at La Fossa (Vulcano, Aeolian Islands, Italy): New insights into seismic sources in a hydrothermal system. Bull Volcanol 72:803–816. https://doi.org/10.1007/s00445-010-0367-6

3. Ardid A, Dempsey D, Caudron C, Cronin S (2022) Seismic precursors to the Whakaari 2019 phreatic eruption are transferable to other eruptions and volcanoes. Nat Commun 13. https://doi.org/10.1038/s41467-022-29681-y

4. Biass S, Bonadonna C, di Traglia F et al (2016) Probabilistic evaluation of the physical impact of future tephra fallout events for the Island of Vulcano, Italy. Bull Volcanol 78:1–22. https://doi.org/10.1007/s00445-016-1028-1

5. Bukumirovic T, Italiano F, Nuccio PM (1997) The evolution of a dynamic geological system: the support of a GIS for geochemical measurements at the fumarole field of Vulcano, Italy

6. Bukumirovic T, Italiano F, Nuccio PM et al (1996) Evolution of the fumarolic activity at La Fossa Crater of Vulcano. Acta Vulcanol 8:210–211

7. Cannata A, Diliberto IS, Alparone S et al (2012) Multiparametric approach in investigating volcano-hydrothermal systems: The case study of Vulcano (Aeolian Islands, Italy). Pure Appl Geophys 169:167–182. https://doi.org/10.1007/s00024-011-0297-z

8. Capasso G, Favara R, Inguaggiato S (1997) Chemical features and isotopic composition of gaseous manifestations on Vulcano Island. An interpretative model of fluid circulation, Aeolian Islands, Italy

9. Capasso G, Inguaggiato S, Nuccio PM et al (1994) Chemical variations in the fumarolic gases of La Fossa di Vulcano crater. Acta Vulcanol 6:41–43

10. Cappello A, Ganci G, Calvari S et al (2016) Lava flow hazard modeling during the 2014–2015 Fogo eruption, Cape Verde. J Geophys Res Solid Earth 121:2290–2303. https://doi.org/10.1002/2015JB012666

11. Carapezza M, Diliberto I (1993) Helium and CO2 soil degassing. Acta Vulcanol 3:273–276

12. Chiodini G, Cioni R (1995) Origin of the fumarolic fluids of Vulcano Island, Italy and implications for volcanic surveillance. Bull Volcanol 57:99–110

13. Chiodini G, Cioni R, Guidi M et al (1998) Soil CO2 flux measurements in volcanic and geothermal areas. Appl Geochem 13:543–552

14. Chiodini G, Granieri D, Avino R et al (2005) Carbon dioxide diffuse degassing and estimation of heat release from volcanic and hydrothermal systems. J Geophys Res Solid Earth 110:1–17. https://doi.org/10.1029/2004JB003542

15. Chouet BA, Matoza RS (2013) A multi-decadal view of seismic methods for detecting precursors of magma movement and eruption. J Volcanol Geoth Res 252:108–175

16. Christenson BW, Reyes AG, Young R et al (2010) Cyclic processes and factors leading to phreatic eruption events: Insights from the 25 September 2007 eruption through Ruapehu Crater Lake, New Zealand. J Volcanol Geoth Res 191:15–32. https://doi.org/10.1016/j.jvolgeores.2010.01.008

17. Clark SP (1966) Thermal conductivity. In: Clark SP (ed) Handbook of Physical Constants, Revised Edition. The Geological Society of America, New York, pp 459–483

18. Coppola D, Laiolo M, Campus A, Massimetti F (2022) Thermal unrest of a fumarolic field tracked using VIIRS imaging bands: The case of La fossa crater (Vulcano Island, Italy). Front Earth Sci (Lausanne) 10. https://doi.org/10.3389/feart.2022.964372

19. de Astis G, Lucchi F, Dellino P et al (2013) Geology, volcanic history and petrology of vulcano (central aeolian archipelago). Geol Soc Mem 37:281–349. https://doi.org/10.1144/M37.11

20. de Fiore O (1924) Brevi note sull'attività di Vulcano (Isole Eolie) dal 1890 al 1924. Bulletin Volcanologique 2

21. de Fiore O (1922) Vulcano (Isole Eolie), Riv. Vulcanologica. Cozzolino, Napoli

22. Diliberto IS (2011) Long-term variations of fumarole temperatures on Vulcano Island (Italy). Ann Geophys 54. https://doi.org/10.4401/ag-5183

23. Diliberto IS (2017) Long-term monitoring on a closed-conduit volcano: A 25 year long time-series of temperatures recorded at La Fossa cone (Vulcano Island, Italy), ranging from 250°C to 520°C. J Volcanol Geoth Res 346:151–160. https://doi.org/10.1016/j.jvolgeores.2017.03.005

24. Dipartimento della Protezione Civile (2021) Vulcano - Variazione attività dal 2021. In: https://rischi.protezionecivile.gov.it/it/vulcanico/vulcani-italia/vulcano

25. Federico C, Capasso G, Paonita A, Favara R (2010) Effects of steam-heating processes on a stratified volcanic aquifer: Stable isotopes and dissolved gases in thermal waters of Vulcano Island (Aeolian archipelago). J Volcanol Geoth Res 192:178–190. https://doi.org/10.1016/j.jvolgeores.2010.02.020

26. Fusillo R, di Traglia F, Gioncada A et al (2015) Deciphering post-caldera volcanism: insight into the Vulcanello (Island of Vulcano, Southern Italy) eruptive activity based on geological and petrological constraints. Bull Volcanol 77. https://doi.org/10.1007/s00445-015-0963-6

27. Galderisi A, Bonadonna C, Delmonaco G et al (2013) Vulnerability assessment and risk mitigation: The case of Vulcano Island, Italy. Landslide Science and Practice: Social and Economic Impact and Policies. Springer Science and Business Media Deutschland GmbH, pp 55–64

28. Gambino S, Guglielmino F (2008) Ground deformation induced by geothermal processes: A model for La Fossa Crater (Vulcano Island, Italy). J Geophys Res Solid Earth 113. https://doi.org/10.1029/2007JB005016

29. Ganci G, Bilotta G, Cappello A et al (2016) HOTSAT: A multiplatform system for the thermal monitoring of volcanic activity using satellite data. Geol Soc Spec Publ 426:207–221. https://doi.org/10.1144/SP426.21

30. Ganci G, Bilotta G, Zuccarello F et al (2023) A Multi-Sensor Satellite Approach to Characterize the Volcanic Deposits Emitted during Etna's Lava Fountaining: The 2020–2022 Study Case. Remote Sens (Basel) 15:916. https://doi.org/10.3390/rs15040916

31. Gangemi MV, Alparone S, Andrea C et al (2022) Analysis of seismic signals accompaignying the unrest of Vulcano in 2021

32. Gaonac'h H, Vandemeulebrouck J, Stix J, Halbwachs M (1994) Thermal infrared satellite measurements of volcanic activity at Stromboli and Vulcano. J Geophys Res 99:9477–9485. https://doi.org/10.1029/93JB02392

33. Geshi N, Iguchi M, Shinohara H (2016) Phreatomagmatic eruptions of 2014 and 2015 in Kuchinoerabujima Volcano triggered by a shallow intrusion of magma. J Nat Disaster Sci 37:67–78

34. Girona T, Realmuto V, Lundgren P (2021) Large-scale thermal unrest of volcanoes for years prior to eruption. Nat Geosci 14:238–241. https://doi.org/10.1038/s41561-021-00705-4

35. Gurioli L, Zanella E, Gioncada A, Sbrana A (2012) The historic magmatic-hydrothermal eruption of the Breccia di Commenda, Vulcano, Italy. Bull Volcanol 74:1235–1254. https://doi.org/10.1007/s00445-012-0590-4

36. Hamling IJ (2017) Crater Lake Controls on Volcano Stability: Insights From White Island, New Zealand. Geophys Res Lett 44:11,311 – 11,319. https://doi.org/10.1002/2017GL075572

37. Harris A (2013) Thermal Remote Sensing of Active Volcanoes. Cambridge University Press

38. Harris A, Alparone S, Bonforte A et al (2012) Vent temperature trends at the Vulcano Fossa fumarole field: The role of permeability. Bull Volcanol 74:1293–1311. https://doi.org/10.1007/s00445-012-0593-1

39. Harris A, Lodato L, Dehn J, Spampinato L (2009) Thermal characterization of the Vulcano fumarole field. Bull Volcanol 71:441–458. https://doi.org/10.1007/s00445-008-0236-8

40. Harris A, Maciejewski A (2000) Thermal surveys of the Vulcano Fossa fumarole field 1994–1999: evidence for fumarole migration and sealing. J Volcanology dGeothermal Res 102:119–147

41. Harris A, Stevenson DS (1997) Thermal observations of degassing open conduits and fumaroles at Stromboli and Vulcano using remotely sensed data

42. Harvey MC, Rowland J, Chiodini G et al (2015) Heat flux from magmatic hydrothermal systems related to availability of fluid recharge. J Volcanol Geoth Res 302:225–236. https://doi.org/10.1016/j.jvolgeores.2015.07.003

43. Heap MJ, Troll VR, Kushnir ARL et al (2019) Hydrothermal alteration of andesitic lava domes can lead to explosive volcanic behaviour. Nat Commun 10. https://doi.org/10.1038/s41467-019-13102-8

44. il Giornale di Lipari (2022) Vulcano: Sindaco chiude alla balneazione spiaggia di levante, abbassamento ph del mare. https://www.giornaledilipari.it/vulcano-sindaco-chiude-alla-balneazione-spiaggia-di-levante-abbassamento-ph-del-mare/. Accessed 1 Oct 2022

45. il Mattino (2022) Vulcano riapre ai turisti dal primo febbraio. «Dati relativi al gas non più preoccupanti». https://www.ilmattino.it/primopiano/cronaca/vulcano_riapre_turisti_febbraio_eolie_gas_cosa_succede_oggi_30_gennaio_2022-6472172.html. Accessed 1 Oct 2022

46. Inguaggiato S, Vita F, Diliberto IS et al (2022a) The Extensive Parameters as a Tool to Monitoring the Volcanic Activity: The Case Study of Vulcano Island (Italy). Remote Sens (Basel) 14:. https://doi.org/10.3390/rs14051283

47. Inguaggiato S, Vita F, Diliberto IS et al (2022b) The volcanic activity changes occurred in the 2021–2022 at Vulcano island (Italy), inferred by the abrupt variations of soil CO2 output. Sci Rep 12:21166. https://doi.org/10.1038/s41598-022-25435-4

48. Istituto Nazionale Di Geofisica e Vulcanologia (2021a) BOLLETTINO MENSILE SUL MONITORAGGIO GEOCHIMICO DELL'ISOLA DI VULCANO Settembre 2021

49. Istituto Nazionale Di Geofisica e Vulcanologia (2021b) BOLLETTINO MENSILE SUL MONITORAGGIO GEOCHIMICO DELL'ISOLA DI VULCANO Luglio 2021

50. Kato A, Terakawa T, Yamanaka Y et al (2015) Preparatory and precursory processes leading up to the 2014 phreatic eruption of Mount Ontake, Japan. Earth Planets and Space 67. https://doi.org/10.1186/s40623-015-0288-x

51. Keller J (1980) THE ISLAND OF VULCANO. Rend Società Italiana di Mineralogia e Petrologia 26:369–414

52. Keszthelyi L, Harris AJL, Dehn J (2003) Observations of the effect of wind on the cooling of active lava flows. Geophys Res Lett 30. https://doi.org/10.1029/2003GL017994

53. Malin MC, Dzurisin D, Sharp RP (1983) Stripping of Keanakakoi tephra on Kilauea Volcano, Hawaii. Geol Soc Am Bull 94:1148. https://doi.org/10.1130/0016-7606(1983)94<1148:SOKTOK>2.0.CO;2

54. Mannen K, Yukutake Y, Kikugawa G et al (2018) Chronology of the 2015 eruption of Hakone volcano, Japan: geological background, mechanism of volcanic unrest and disaster mitigation measures during the crisis. Earth Planets and Space 70. https://doi.org/10.1186/s40623-018-0844-2

55. Mannini S, Harris AJL, Jessop DE et al (2019) Combining Ground- and ASTER-Based Thermal Measurements to Constrain Fumarole Field Heat Budgets: The Case of Vulcano Fossa 2000–2019. Geophys Res Lett 46:11868–11877. https://doi.org/10.1029/2019GL084013

56. Matsushima N, Kazahaya K, Saito G, Shinohara H (2003) Mass and heat flux of volcanic gas discharging from the summit crater of Iwodake volcano, Satsuma-Iwojima, Japan, during 1996–1999. J Volcanol Geoth Res 126:285–301. https://doi.org/10.1016/S0377-0273(03)00152-5

57. Mayer K, Scheu B, Yilmaz TI et al (2017) Phreatic activity and hydrothermal alteration in the Valley of Desolation, Dominica, Lesser Antilles. Bull Volcanol 79. https://doi.org/10.1007/s00445-017-1166-0

58. Mazzuoli R, Tortorici L, Ventura G (1995) Oblique rifting in Salina, Lipari and Vulcano islands (Aeolian islands, southern Italy). Terra Nova 7:444–452

59. Mercalli G (1907) Vulcani attivi della terra: morfologia–dinamismo–prodotti–distribuzione. geografica–cause… U. Hoepli

60. Mercalli G (1883) Isola Vulcano. In: Arnaldo F (ed) Vulcani e Fenomeni Vulcanici in Italia. Biblioteca di Sismologia, Milanno, pp 146–162

61. Mercalli G, Silvestri O (1891) L'eruzione dell'Isola di Vulcano incominciata il 3 agosto 1888 e terminata il 22 marzo 1890. Annali dell'ufficio Centrale di Meteorologia e Geodinamica 10:71–281

62. Mick E, Stix J, de Moor JM, Avard G (2021) Hydrothermal alteration and sealing at Turrialba volcano, Costa Rica, as a mechanism for phreatic eruption triggering. J Volcanol Geoth Res. https://doi.org/10.1016/j.jvolgeores.2021.107297. 416:

63. Montalto A (1994) Seismic events at Vulcano (Italy) during 1988–1992. J Volcanol Geoth Res 60:193–206

64. Montanaro C, Mick E, Salas-Navarro J et al (2022) Phreatic and Hydrothermal Eruptions: From Overlooked to Looking Over. https://doi.org/10.1007/s00445-022-01571-7. Bull Volcanol 84:

65. Moretti R, Komorowski JC, Ucciani G et al (2020) The 2018 unrest phase at La Soufrière of Guadeloupe (French West Indies) andesitic volcano: Scrutiny of a failed but prodromal phreatic eruption. J Volcanol Geoth Res. https://doi.org/10.1016/j.jvolgeores.2020.106769. 393:

66. Nakano M, Kumagai H (2005) Response of a hydrothermal system to magmatic heat inferred from temporal variations in the complex frequencies of long-period events at Kusatsu-Shirane Volcano, Japan. J Volcanol Geoth Res 147:233–244. https://doi.org/10.1016/j.jvolgeores.2005.04.003

67. NASA Jet Propulsion Laboratory (2022) EOS and Terra. In: https://asterweb.jpl.nasa.gov/eos.asp

68. Paonita A, Federico C, Bonfanti P et al (2013) The episodic and abrupt geochemical changes at La Fossa fumaroles (Vulcano Island, Italy) and related constraints on the dynamics, structure, and compositions of the magmatic system. Geochim Cosmochim Acta 120:158–178. https://doi.org/10.1016/j.gca.2013.06.015

69. Protezione Civile di Lipari (2021a) Ordinanza Sindaco Lipari n°114 (13/10/2021)

70. Protezione Civile di Lipari (2021b) Ordinanza Sindaco Lipari n°115 (14/10/2021)

71. Protezione Civile di Lipari (2021c) Ordinanza Sindaco Lipari n°124 (20/11/2021)

72. Protezione Civile di Lipari (2021d) Ordinanza Sindaco Lipari n°123 (18/11/2021)

73. Ramsey MS (2016) Synergistic use of satellite thermal detection and science: A decadal perspective using ASTER. Geol Soc Spec Publ 426:115–136. https://doi.org/10.1144/SP426.23

74. Rogic N, Cappello A, Ganci G et al (2019) Spaceborne EO and a combination of inverse and forward modelling for monitoring lava flow advance. Remote Sens (Basel) 11. https://doi.org/10.3390/rs11243032

75. Scolamacchia T, Cronin SJ (2016) Idiosyncrasies of volcanic sulfur viscosity and the triggering of unheralded volcanic eruptions. Front Earth Sci (Lausanne) 4. https://doi.org/10.3389/feart.2016.00024

76. Sekioka M, Yuhara K (1974) Heat flux estimation in geothermal areas based on the heat balance of the ground surface. J Geophys Res 79:2053–2058. https://doi.org/10.1029/jb079i014p02053

77. Selva J, Bonadonna C, Branca S et al (2020) Multiple hazards and paths to eruptions: A review of the volcanic system of Vulcano (Aeolian Islands, Italy). Earth Sci Rev 207

78. Sicardi L (1940) Il recente ciclo dell' attività fumarolica dell' isola di Vulcano. Bull Volcanologique 7:85–139. https://doi.org/10.1007/BF02994895

79. Silvestri M, Rabuffi F, Pisciotta A et al (2019) Analysis of thermal anomalies in volcanic areas using multiscale and multitemporal monitoring: Vulcano Island test case. Remote Sens (Basel) 11. https://doi.org/10.3390/rs11020134

80. Sorey ML, Farrar CD, Gerlach TM et al (2000) Invisible CO2 Gas Killing Trees at Mammoth Mountain, California. US Geological Survey Fact Sheet 172 – 96

81. Stix J, de Moor JM (2018) Understanding and forecasting phreatic eruptions driven by magmatic degassing. Earth Planets and Space 70. https://doi.org/10.1186/s40623-018-0855-z

82. Sutawidjaja IS, Prambada O, Siregar DA (2013) The August 2010 Phreatic Eruption of Mount Sinabung, North Sumatra. Indonesian J Geol 8:55–61. https://doi.org/10.17014/ijog.8.1.55-61

83. Tedesco D, Miele G, Sanob Y, Toutain JP (1995) Helium isotopic ratio in Vulcan0 island fumaroles: temporal variations in shallow level mixing and deep magmatic supply

84. Tedesco D, Toutain JP, Allard P, Losno R (1991) Chemical variations in fumarolic gases at Vulcano Island. seasonal and volcanic effects, Southern Italy)

85. TERRA (2022) ASTER. In: https://terra.nasa.gov/about/terra-instruments/aster

86. USGS (2022a) ASTER Overview. In: https://lpdaac.usgs.gov/data/get-started-data/collection-overview/missions/aster-overview/

87. USGS (2022b) AST_08v003. In: https://lpdaac.usgs.gov/products/ast_08v003/

88. Ventura G (1994) Tectonics, structural evolution and caldera formation on Vulcano Island (Aeolian Archipelago, southern Tyrrhenian Sea). J Volcanol Geoth Res 60:207–224

89. Wolfe RE, Lin G, Nishihama M et al (2013) Suomi NPP VIIRS prelaunch and on-orbit geometric calibration and characterization. J Geophys Res Atmos 118 :11,508 – 11,521. https://doi.org/10.1002/jgrd.50873

90. Wright R, Flynn L, Garbeil H et al (2002) Automated volcanic eruption detection using MODIS. Remote Sens Environ 82:135–155. https://doi.org/https://doi.org/10.1016/S0034-4257(02)00030-5

91. Zuccarello F, Bilotta G, Cappello A, Ganci G (2022) Effusion Rates on Mt. Etna and Their Influence on Lava Flow Hazard Assessment. Remote Sens (Basel) 14:. https://doi.org/10.3390/rs14061366
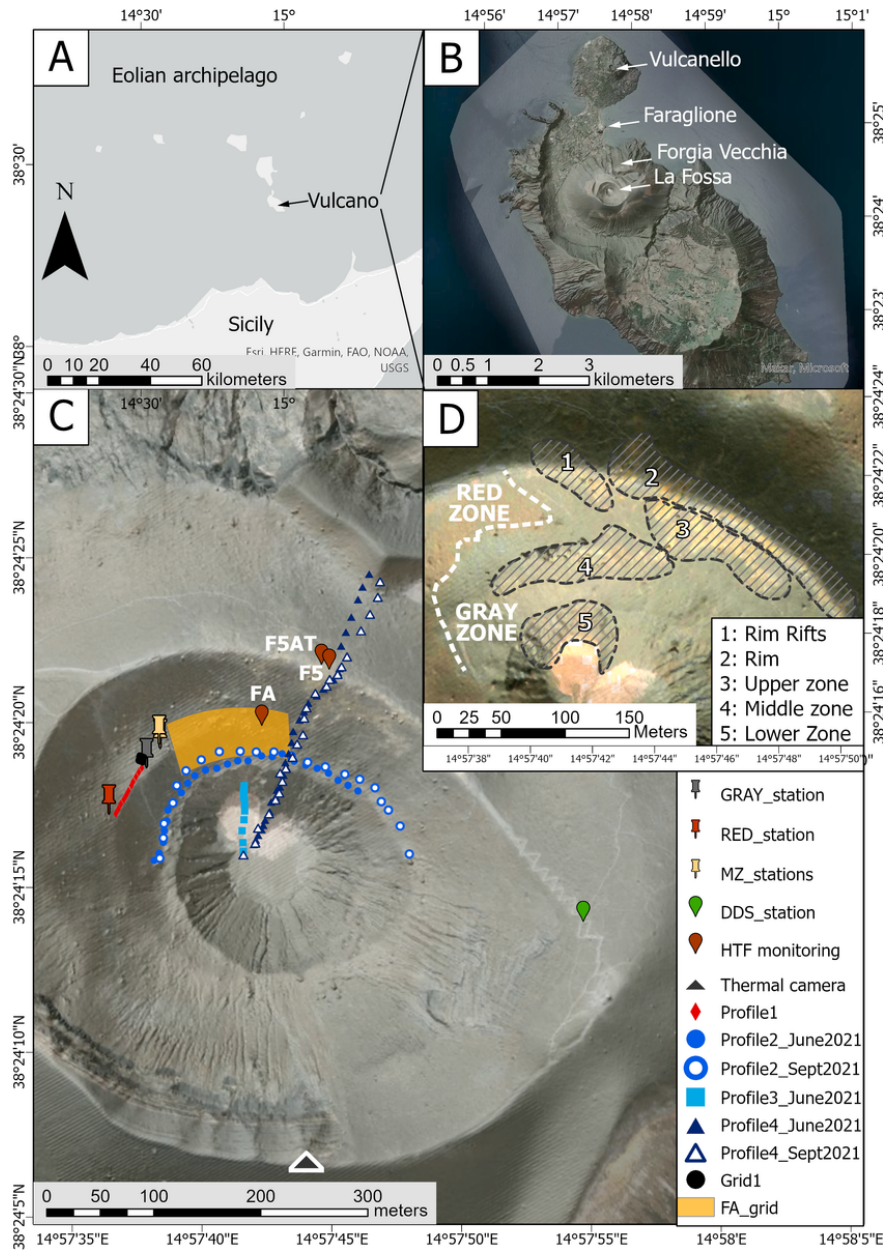
Figures

Figure 1

(A) Location of Vulcano island in the Eolian Archipelago, Sicily. (B) Areas of interest in Vulcano island. (C) Location of permanent stations and punctual measurements. (D) Limit between hot (GRAY) and cold (RED) zones, and the five zones of intense fumaroles release. HTF = High Temperature Fumarole being F5AT, F5 and FA.
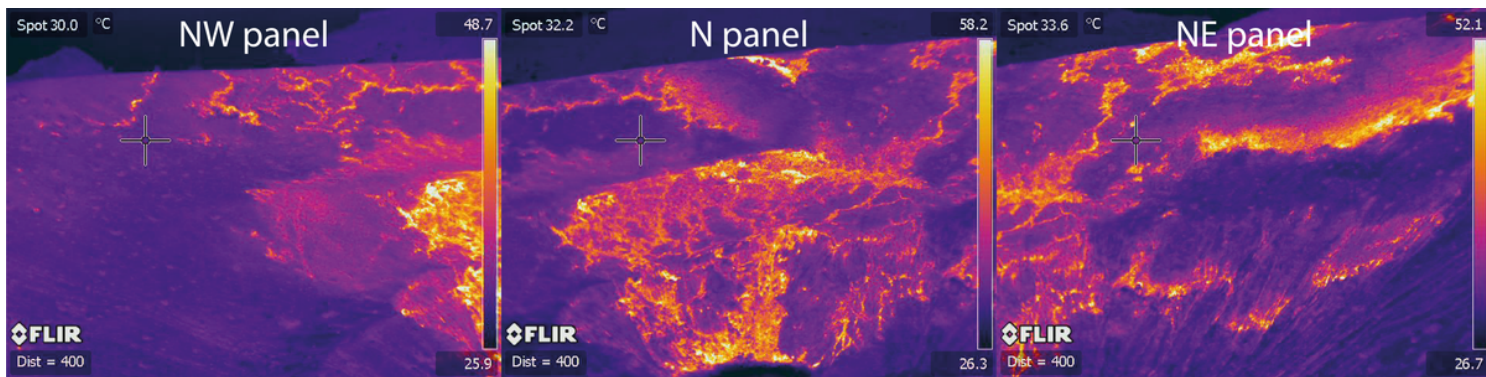
Figure 2

Three thermal image panels. The panels were used to reconstruct the panorama of the entire fumarole field and surrounding heated ground areas on the northern sector of the crater.
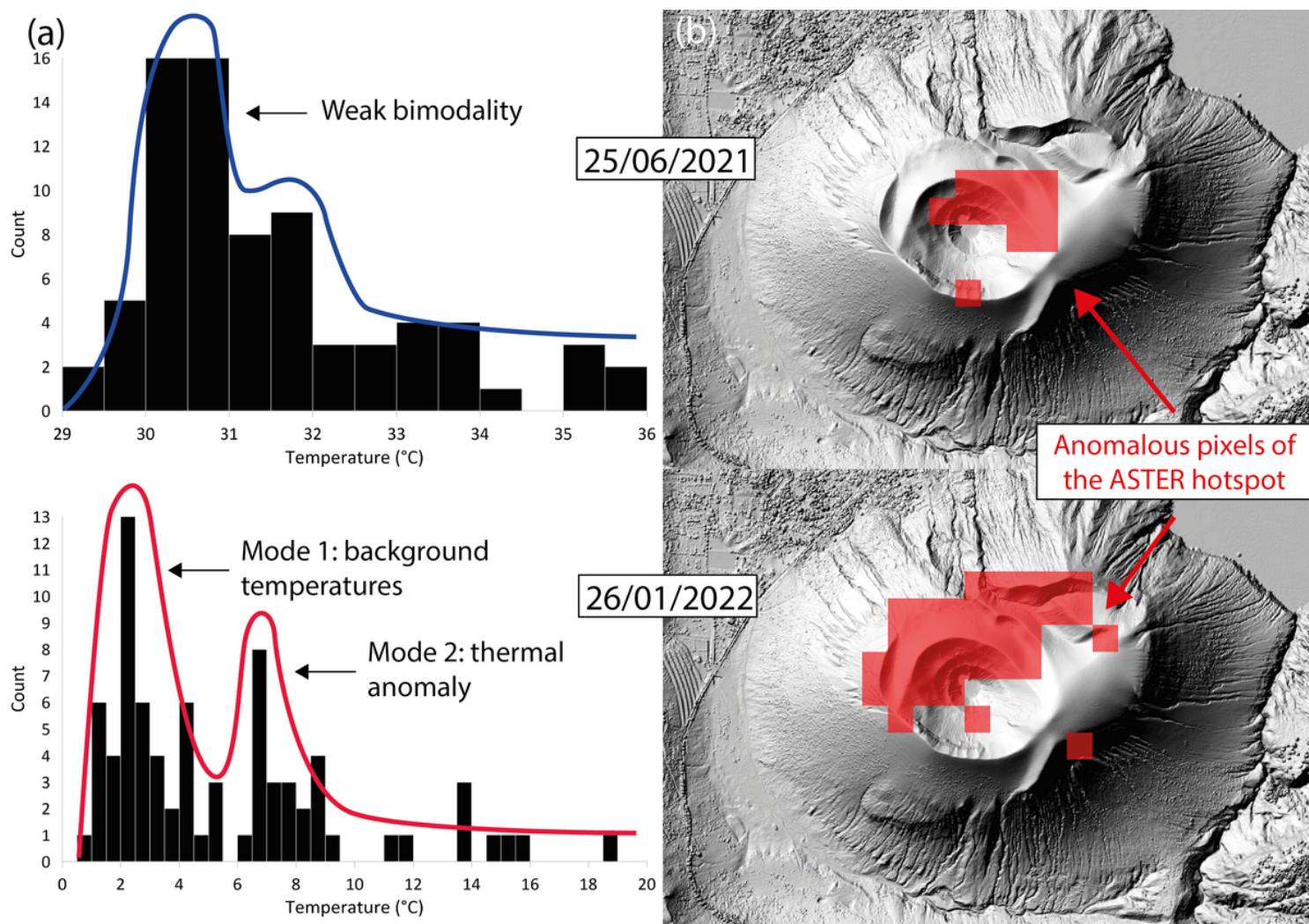
Figure 3

(a) Examples of surface temperature frequency distribution on ASTER images. The distribution starts weakly bimodal with a positive tail and the bimodality increases along with the thermal anomaly. Mode 1 is interpreted as the background reference temperature and mode 2 as the anomalous temperature in the ROI area. (b) Examples of anomalous pixel locations selected following the temperature frequency distribution.
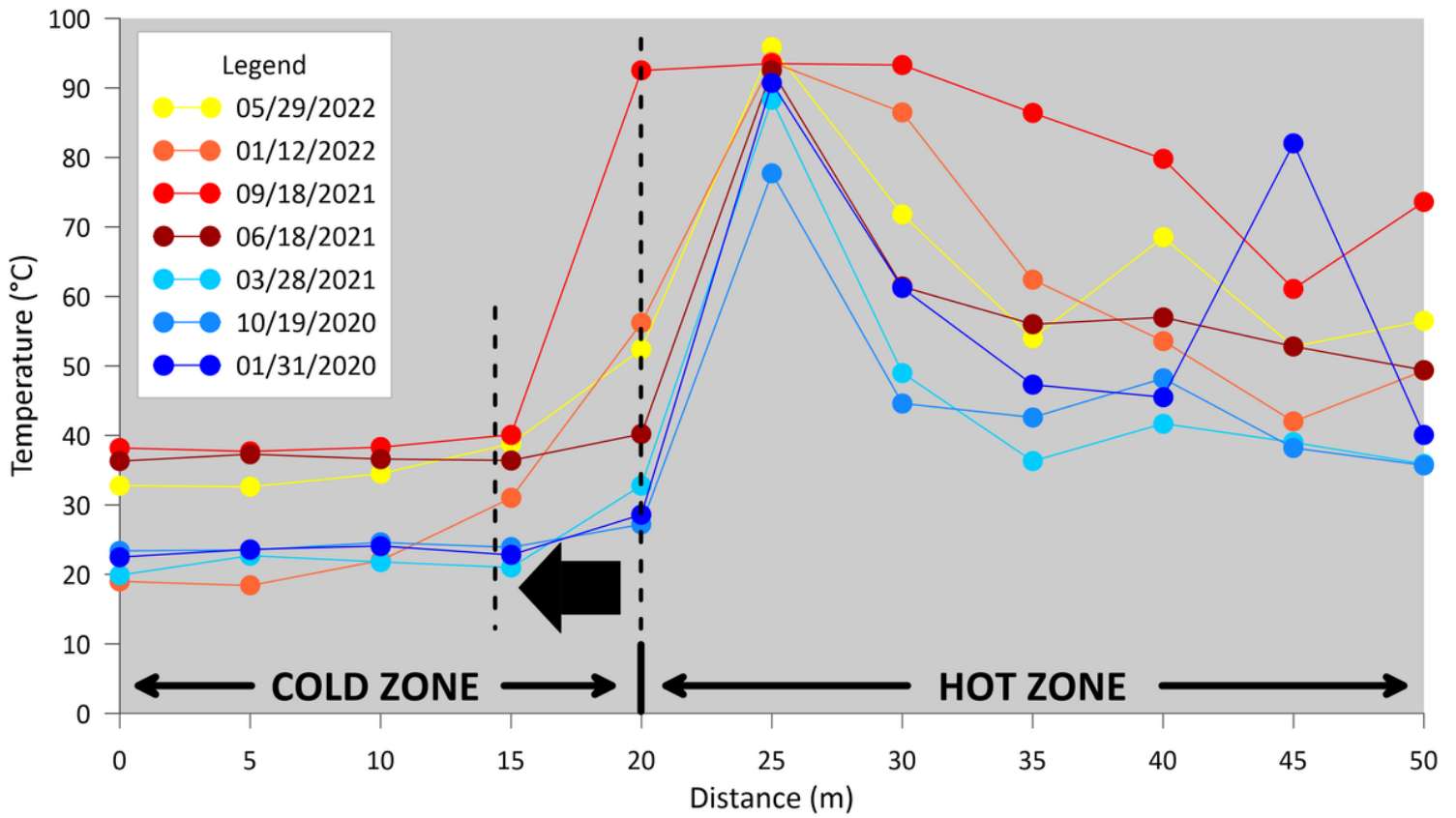
Figure 4

Temperature at 15 cm depth on Profile1 west of the fumarole field (2019-2022) (see Figure 1C for location). The large black arrow marks the hot zone offset into the cold zone after September 2021.
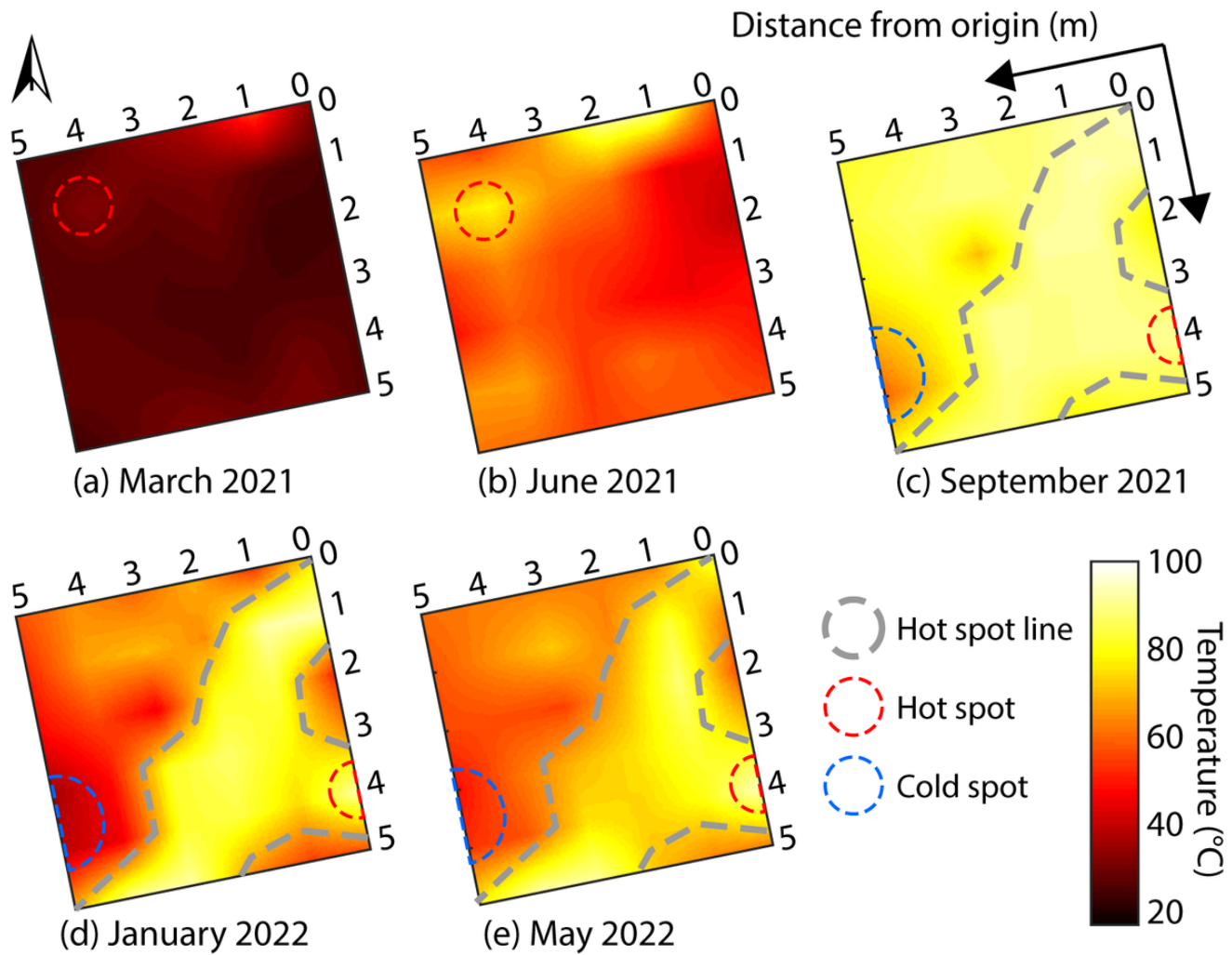
Figure 5

T_{15} for Grid 1 (see Figure 1C for location). Measurement points are interpolated with the nearest neighbor method. The hot and cold spots, either persistent or occasional, and the hot zone that runs diagonally across the area after June 2021 are indicated in the relative survey.
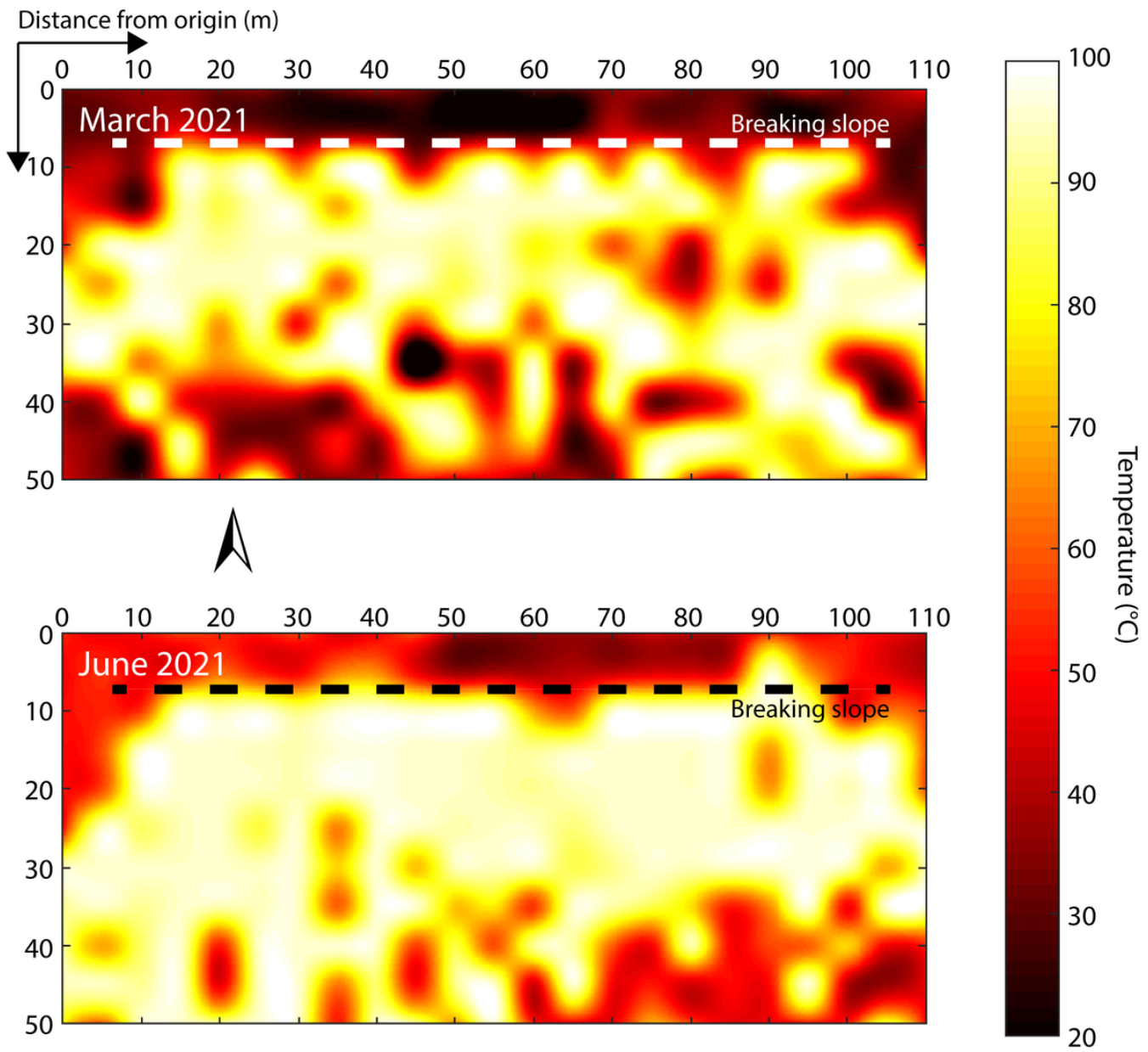
Figure 6

T_{15} for FA grid (see Figure 1C for location).
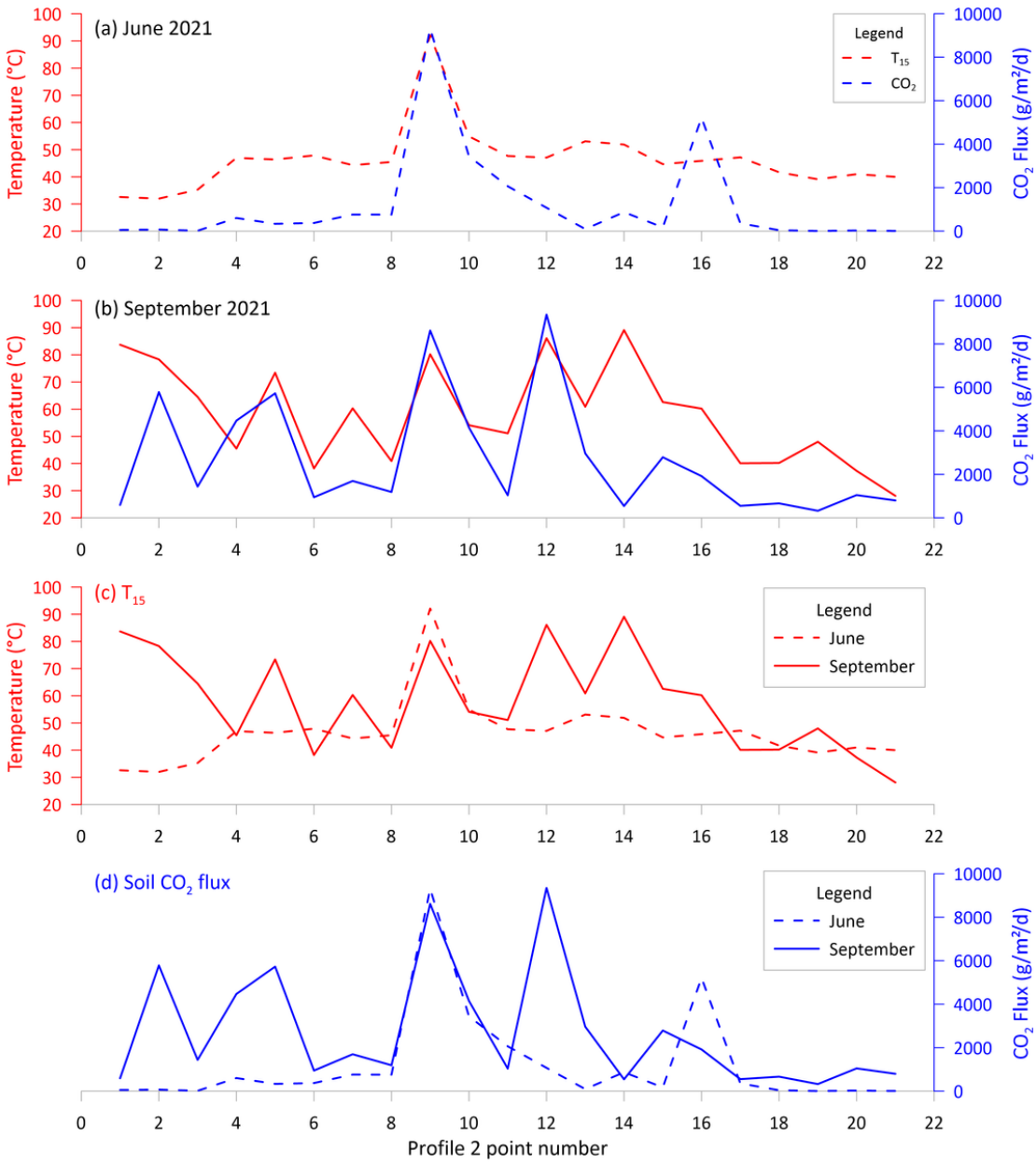
Figure 7

Soil CO_2 flux and T_{15} on Profile2 in (a) June and (b) September 2021. (c) T_{15} in June and September 2021. (d) Soil CO_2 flux in June and September 2021
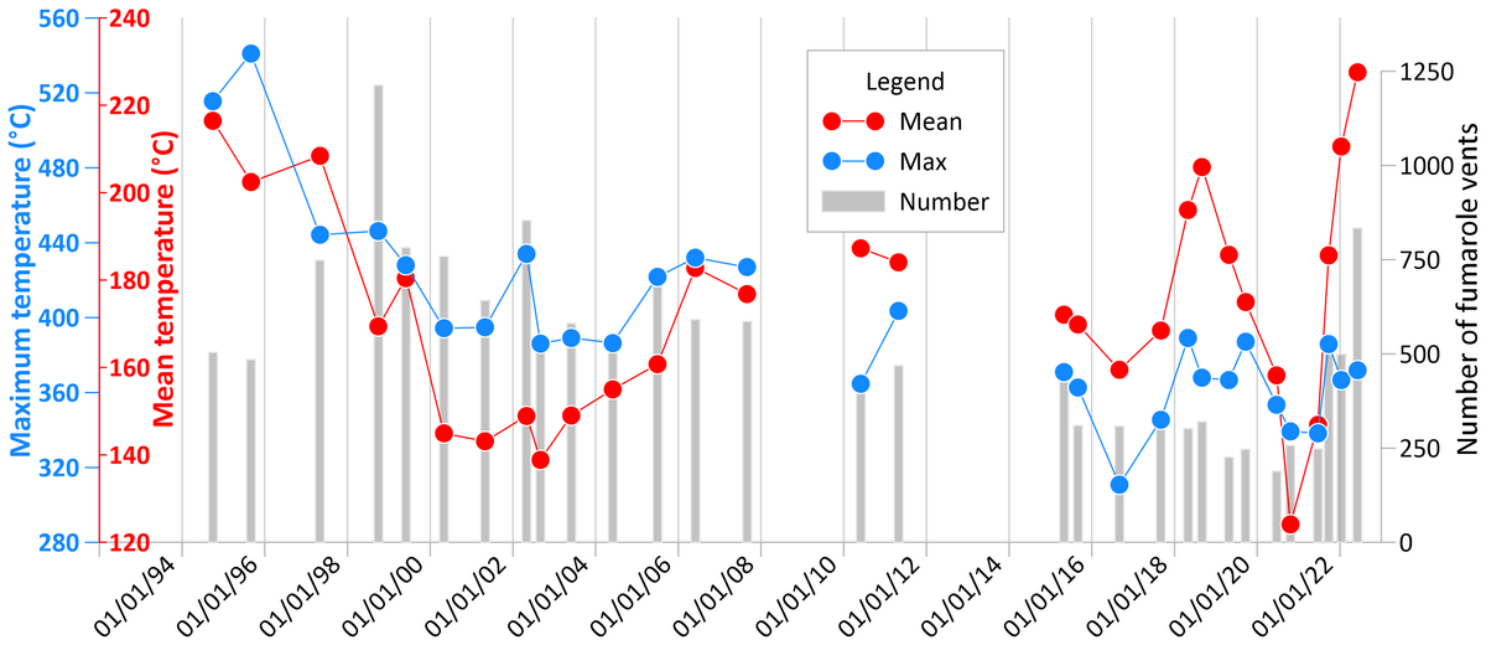
Figure 8

Average and maximum temperature of the Fossa fumarole vents. The lines on the plots are interrupted when the gap between two surveys is higher than one year.
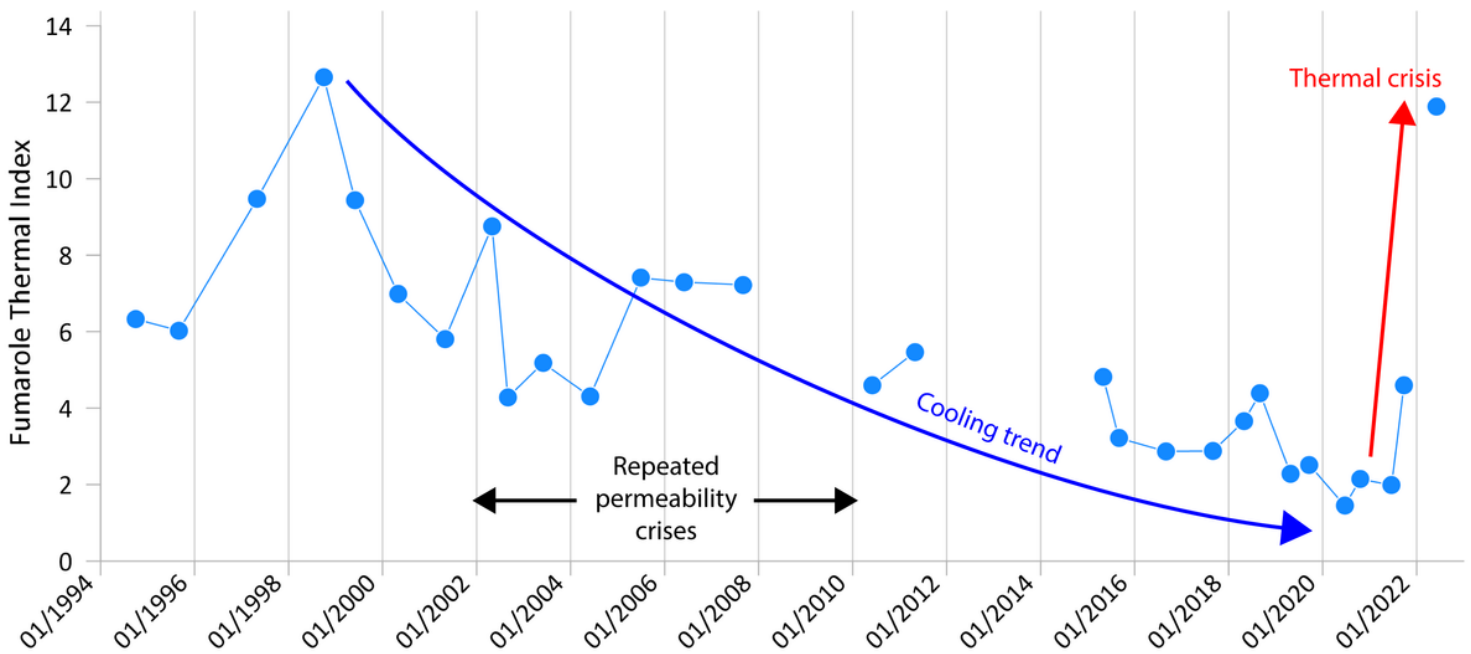
Figure 9

Long term thermal trend of the Fossa fumarole vents. Gaps are when the period of time between two surveys is greater than one year. The point for January 2022 was likely underestimated due to poor visibility (plume condensation).
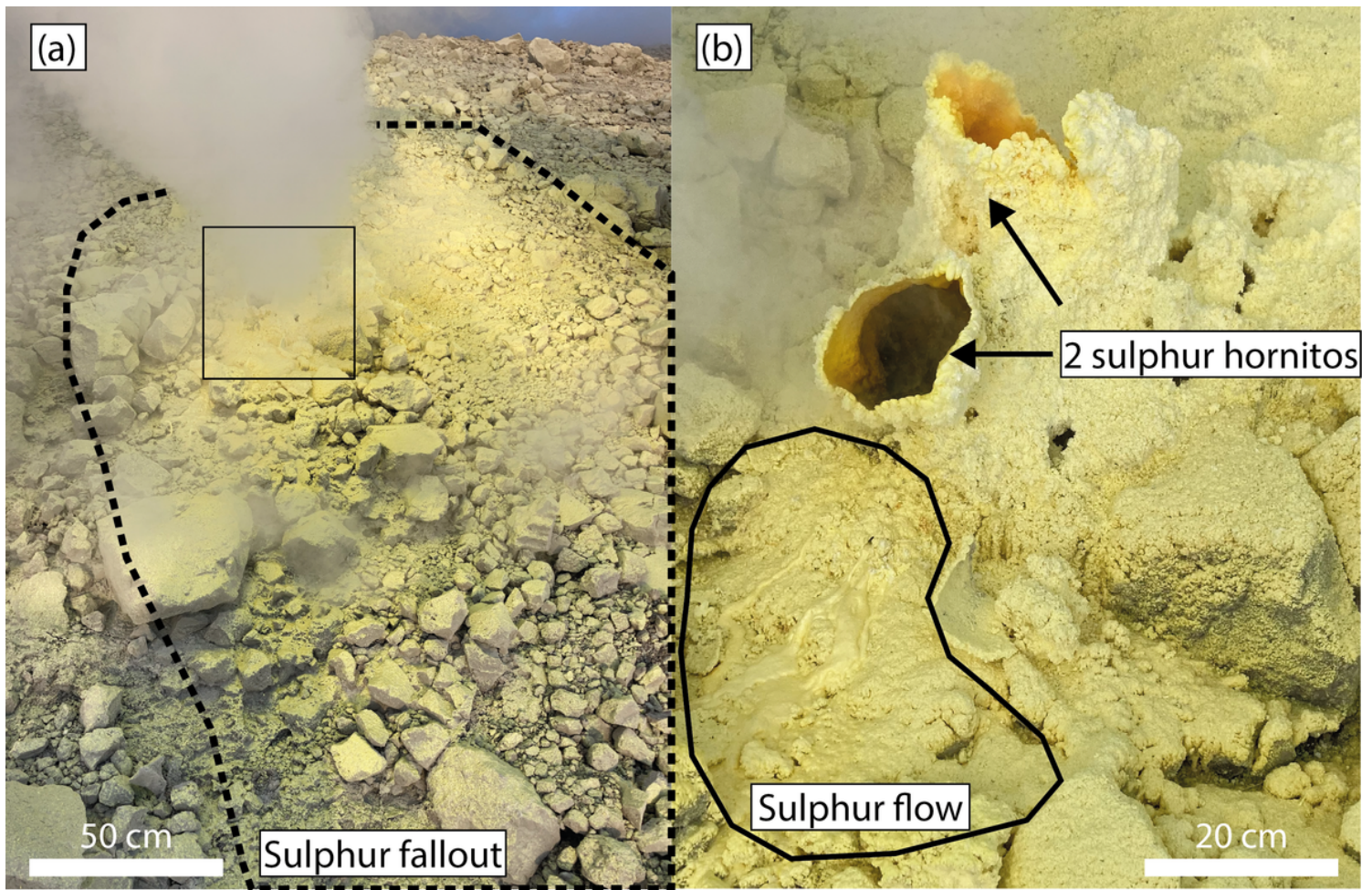
Figure 10

Sulphur hornitos and associated sulfur fallout and flows inside the Fossa fumarole field on 12/01/2022; (b) is the enlargement of the black square showing the details that in (a) are hidden by fume.
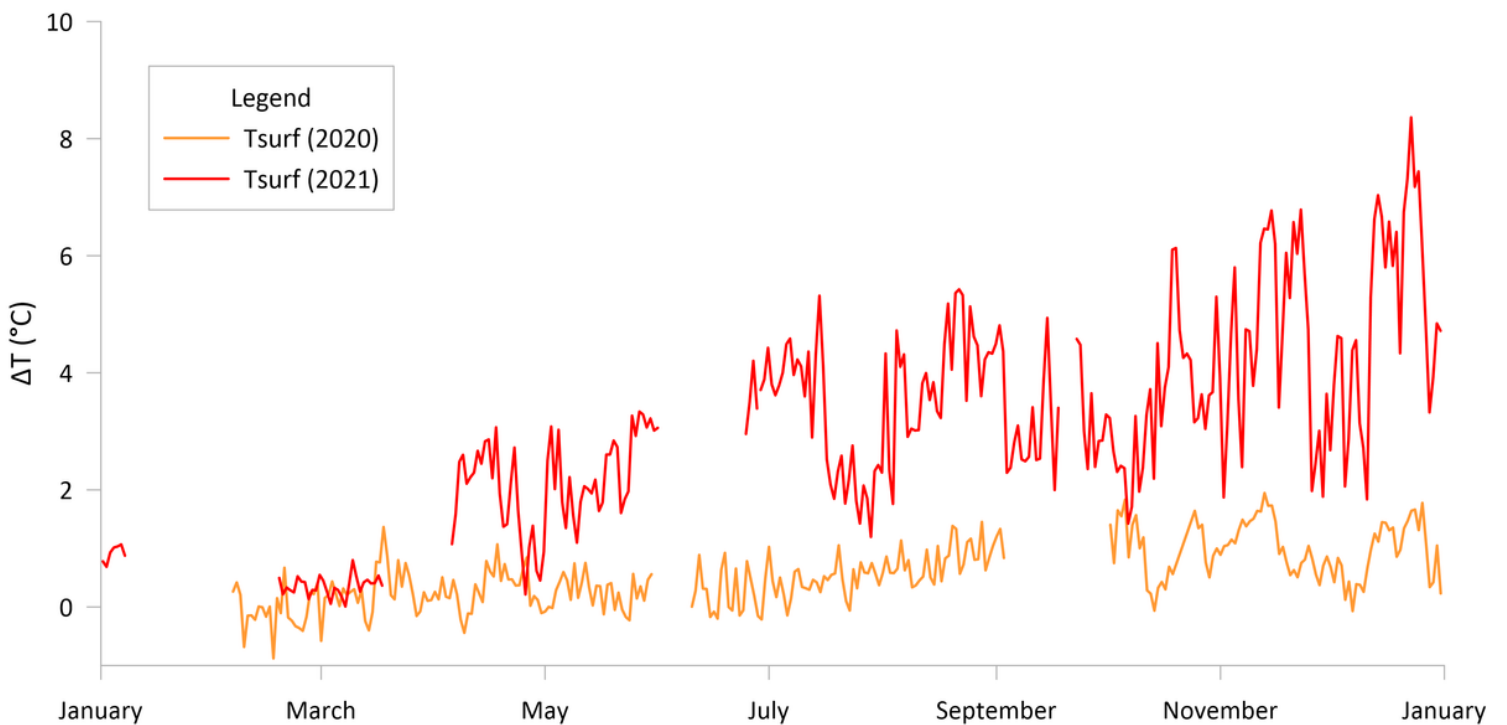
Figure 11

Surface temperature minus air temperature at GRAY station for 2020 and 2021.
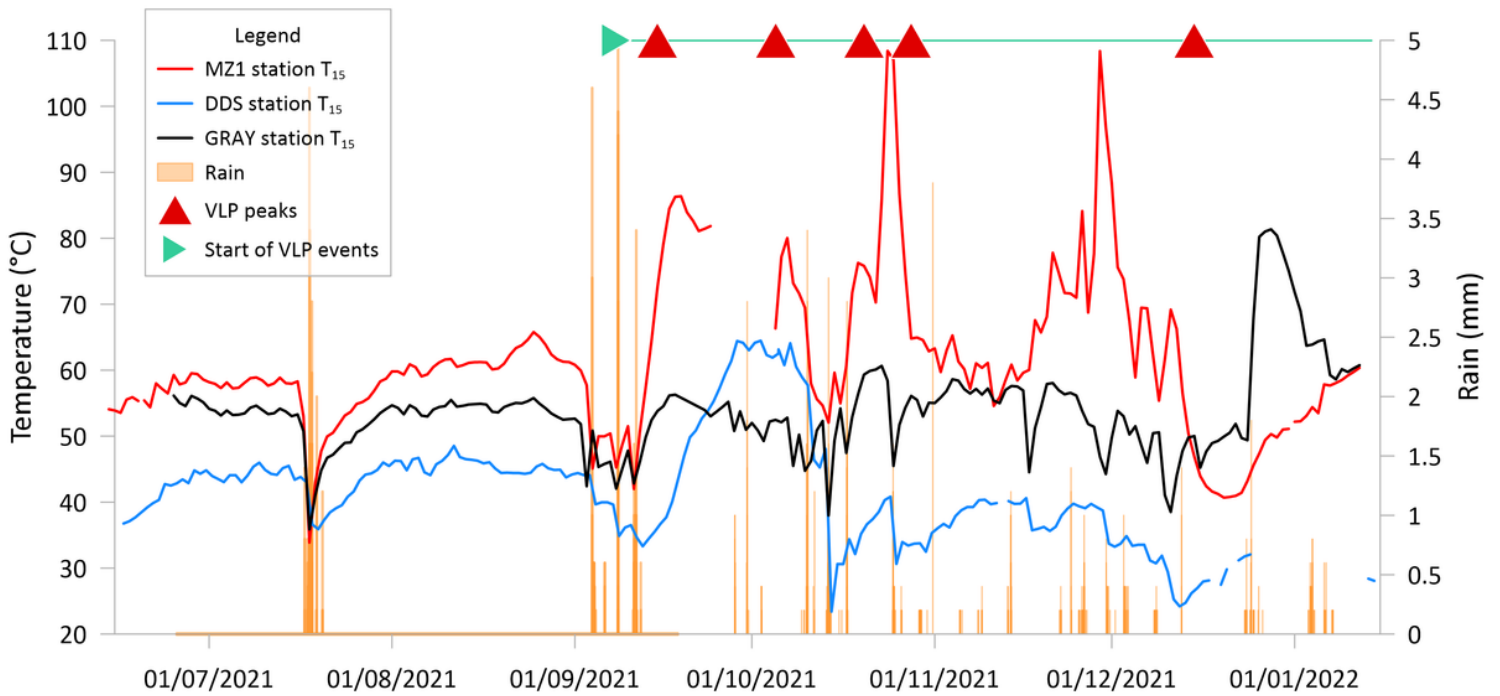
Figure 12

T_{15} and rainfall at MZ1, GRAY and DDS stations. The red triangles indicate VLP event peaks and the green line shows the onset and continuation of seismic activity registered during the unrest (Federico et al., submitted). Many temperature peaks appear synchronous with the peaks in the VLP swarms.
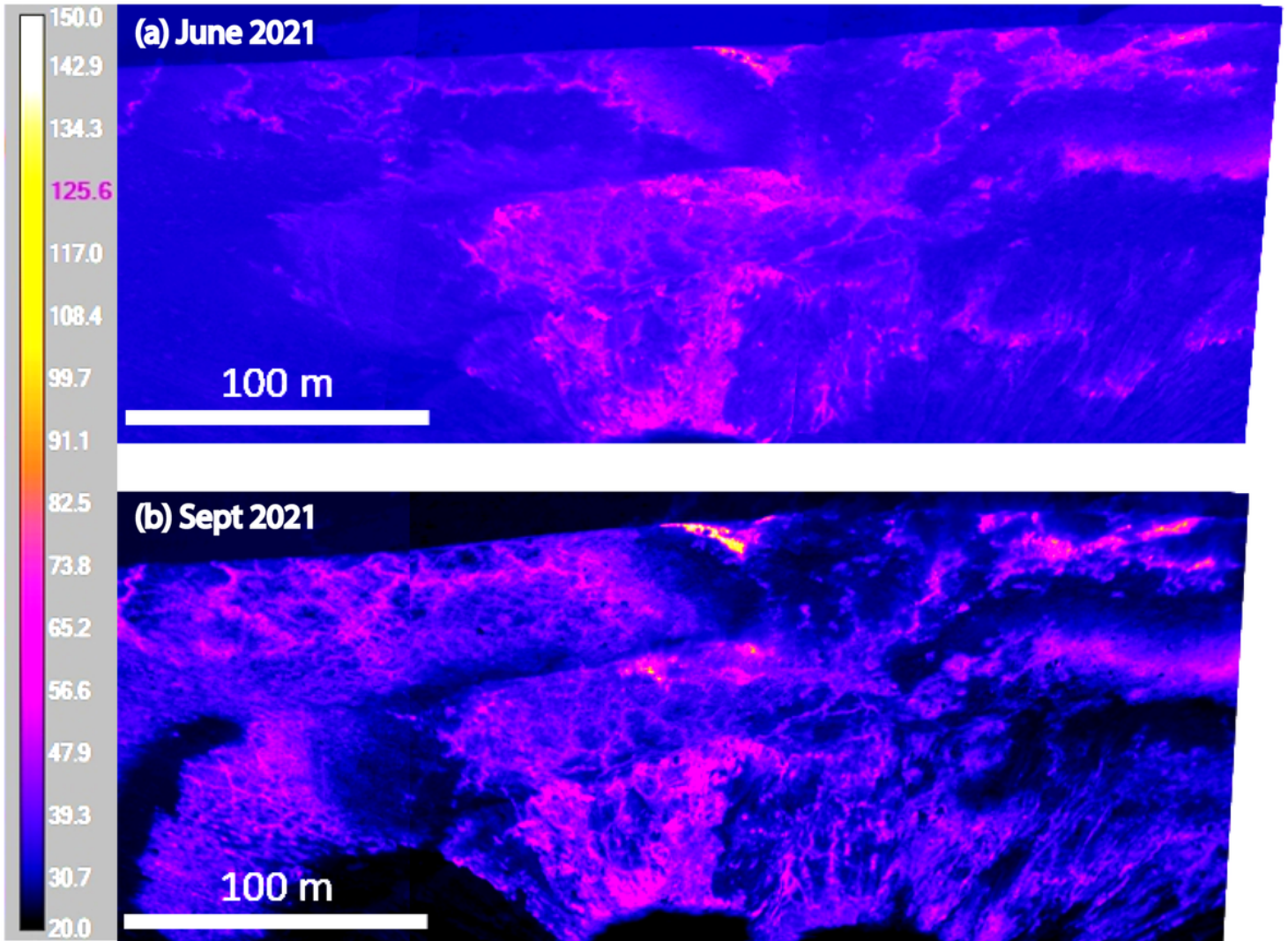
Figure 13

Expansion of the thermal anomaly associated with the fumarole field between (a) June and (b) September 2021 viewed from the thermal camera location (see Figure 1C). The rim zone is not visible from this viewpoint.
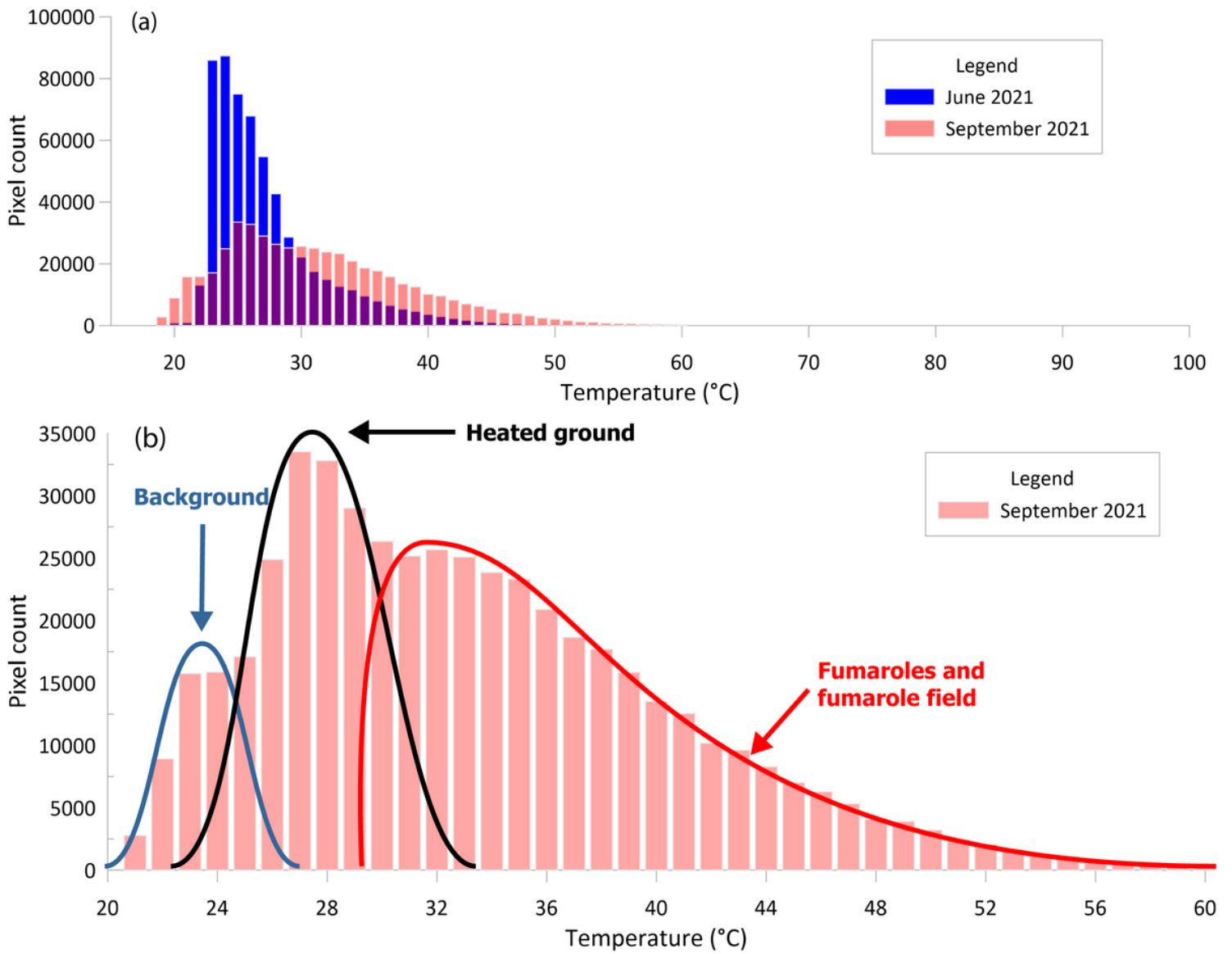
Figure 14

(a) Comparison of surface temperature frequency distributions from thermal camera images obtained in June and September 2021. (b) Surface temperature frequency distribution in September 2021. In (a), air temperature has been subtracted from surface temperature and to avoid bias due to different background temperatures, the first bins of the temperature distributions have been fitted to each other. This is achieved by adding 25 °C to all bins in the June 2021 distribution. The effectively accounts for seasonal effects on surface temperatures.
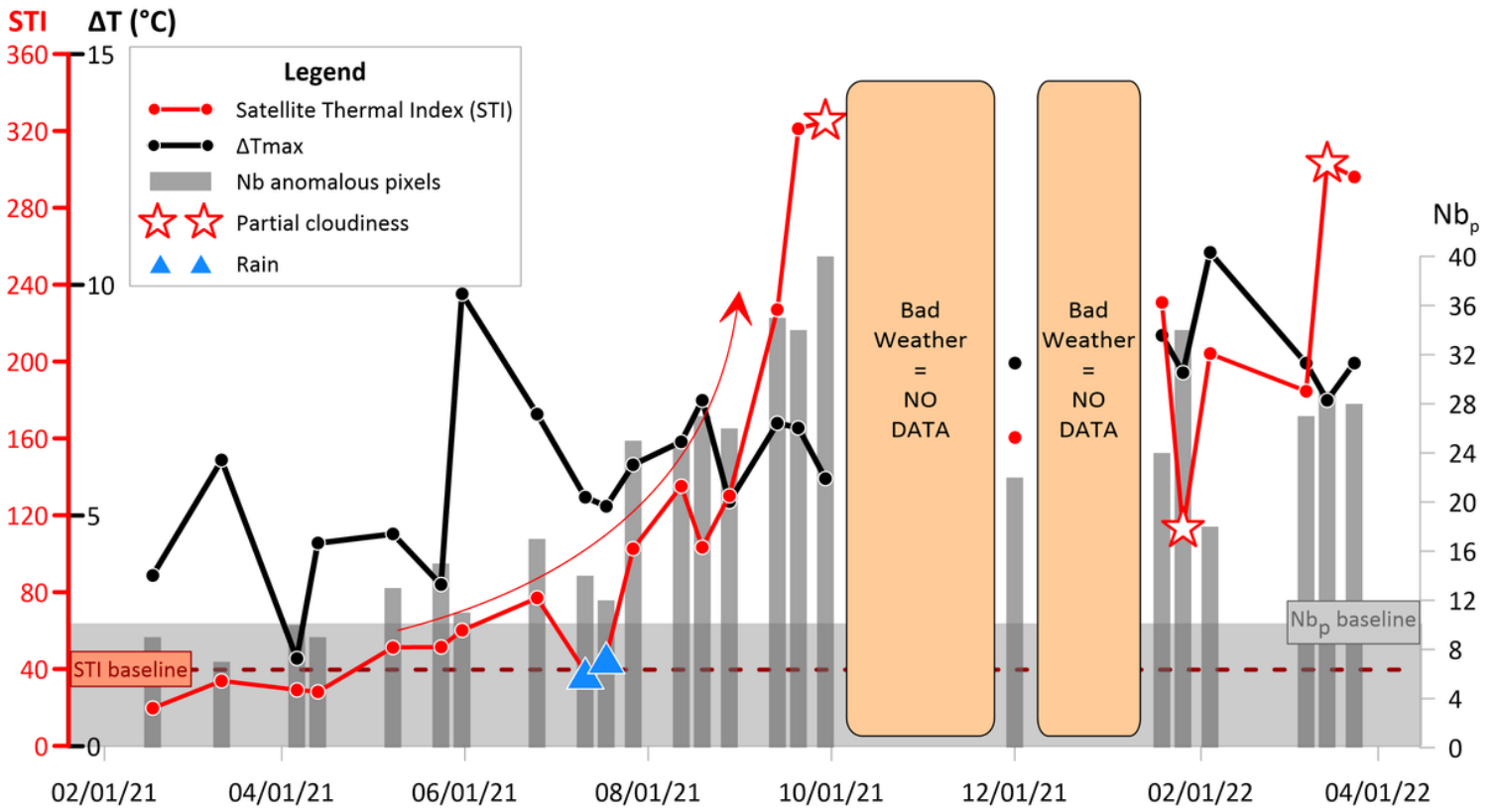
Figure 15

ASTER-derived thermal indices. Three scenes (09/29/21, 01/26/22 and 03/14/22) were still selected even though the cloud cover was partially covering the crater (colored star mark). The July 2021 storm events are marked by a blue triangle. The STI and NB_p baselines are respectively placed at 40 and 10 pixels.
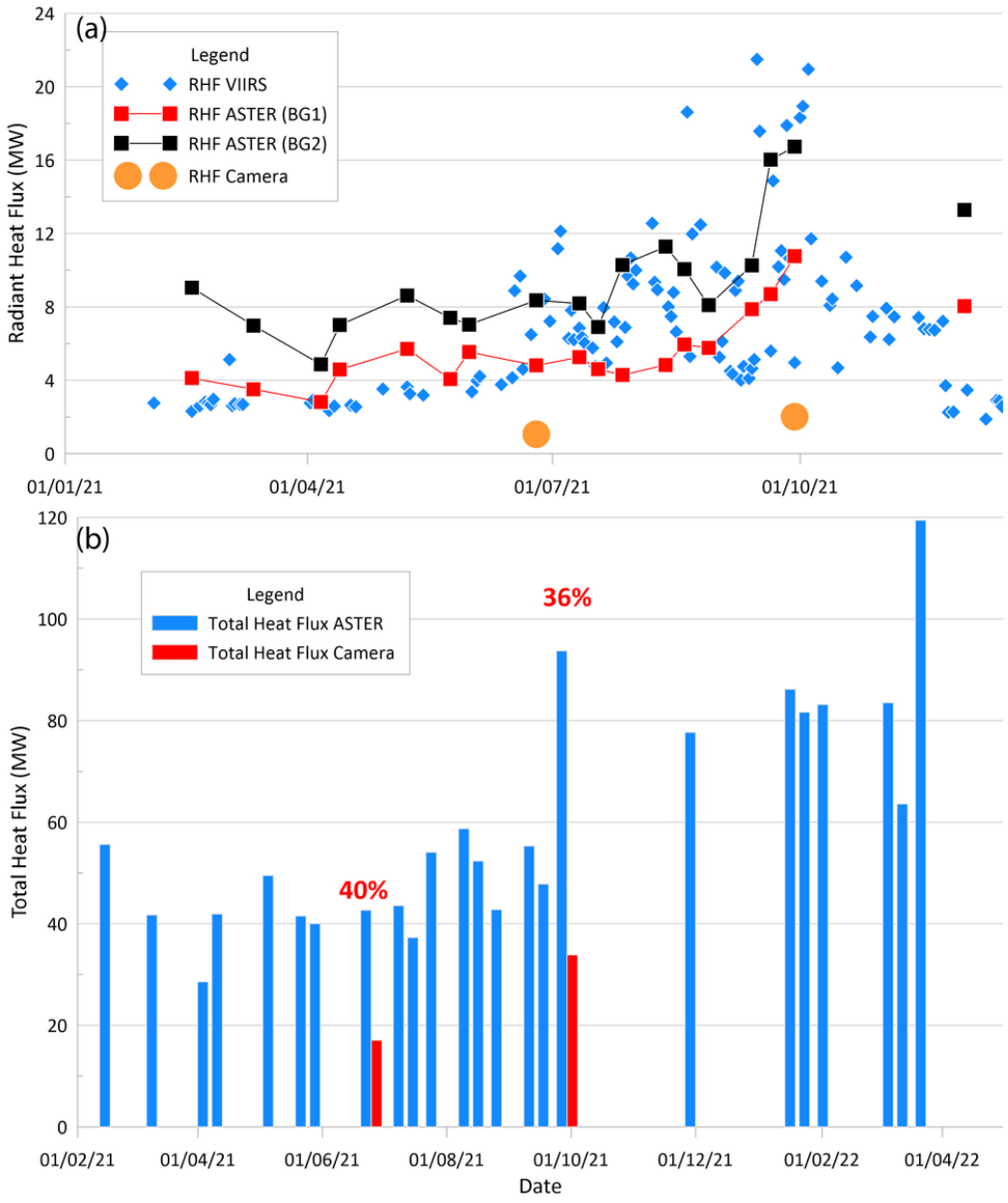
Figure 16

(a) Comparison of Radiative Heat Flux (RHF) from ASTER, VIIRS and ground-based thermal imagery. Minimum bound for ASTER heat flux is using the first mode of temperature distribution for pixels in the Fossa ROI as background temperature (BG1). Maximum bound uses the minimum temperature from the same ROI (BG2). (b) Total heat flux time series as calculated from ASTER on the whole exposed anomaly. The total heat flux is compared to the heat flux from ground-based thermal imagery (targeting only the inner flank of the northern slope).

Figure 17

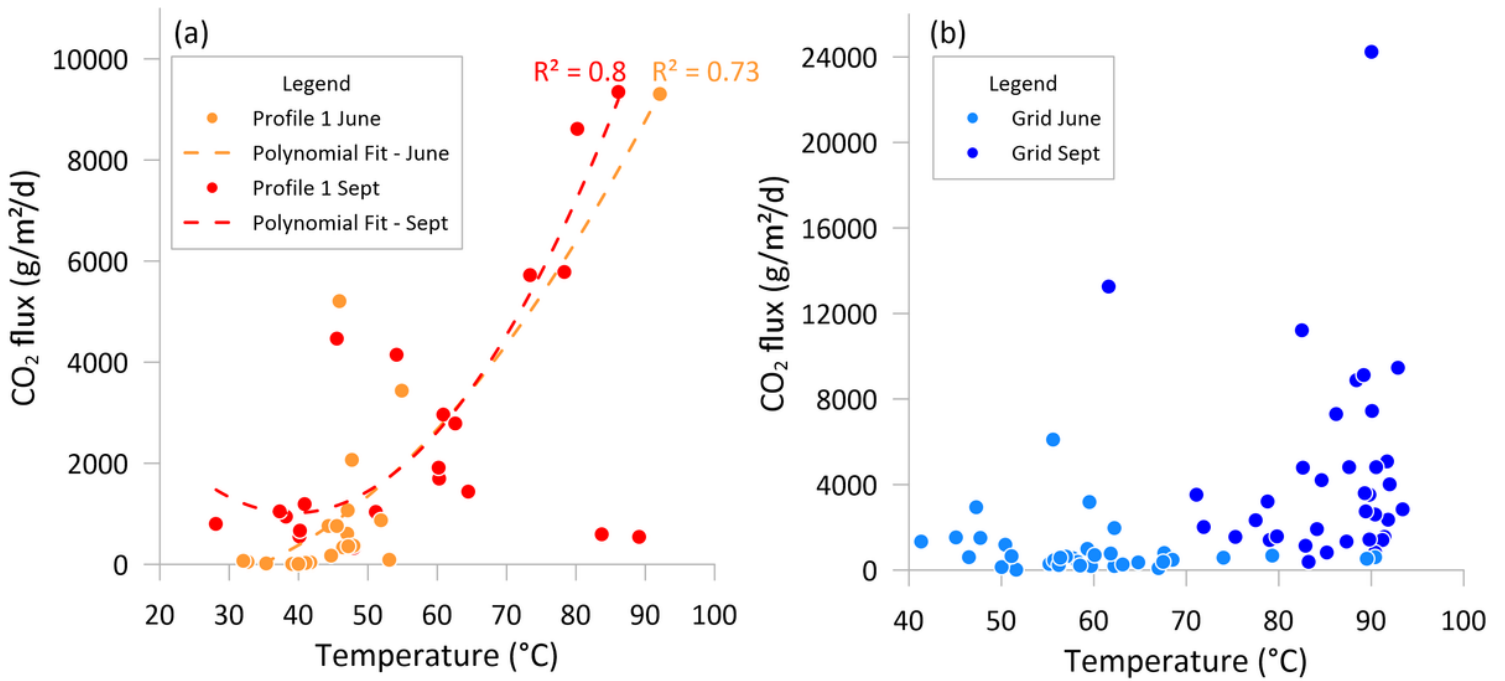Stressed vegetation on the south rim of La Fossa crater in January 2021. White rectangle is magnified top left.

Figure 18

(a) Comparison of T_{15} and soil CO_2 flux along Profile 1 and (b) across Grid 1
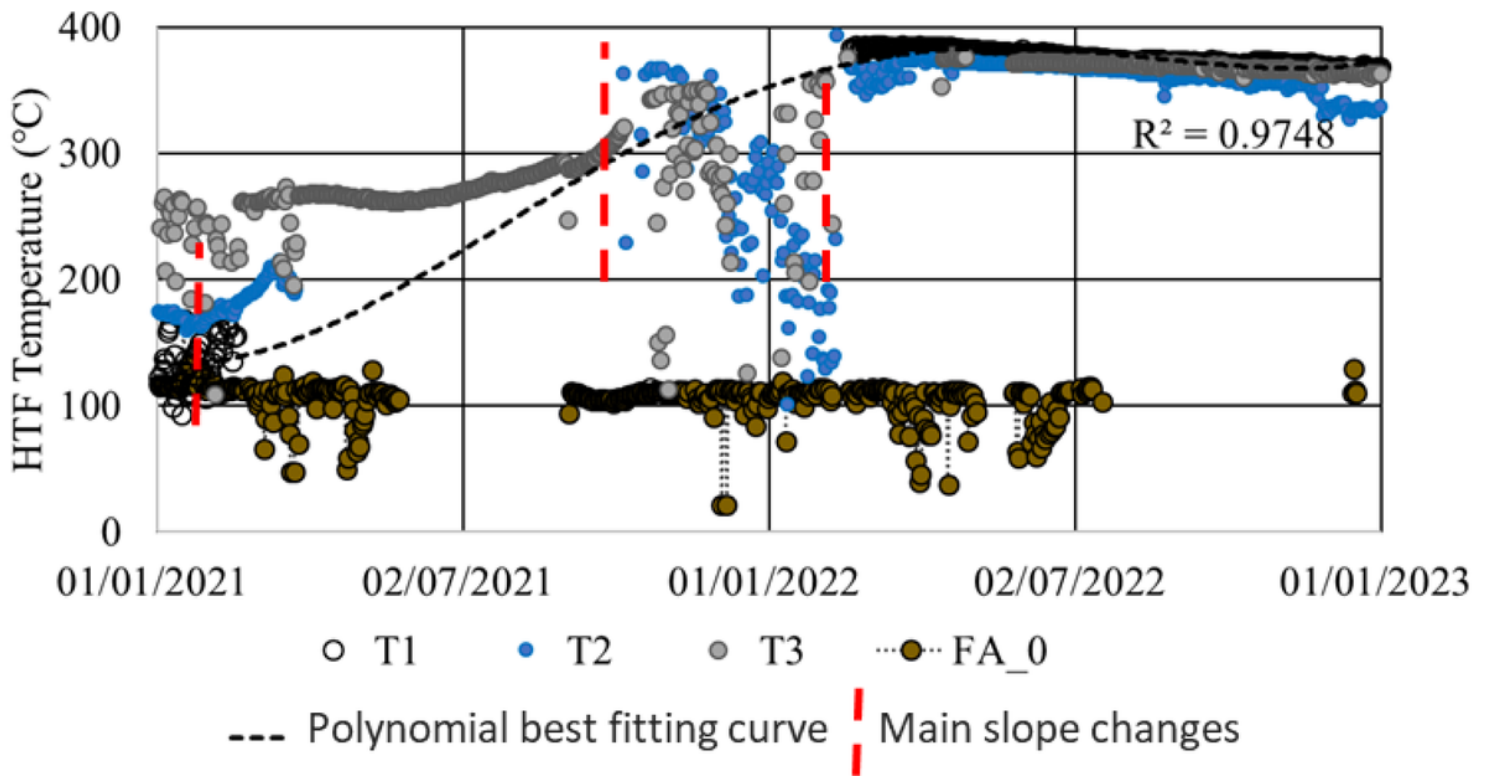
Figure 19

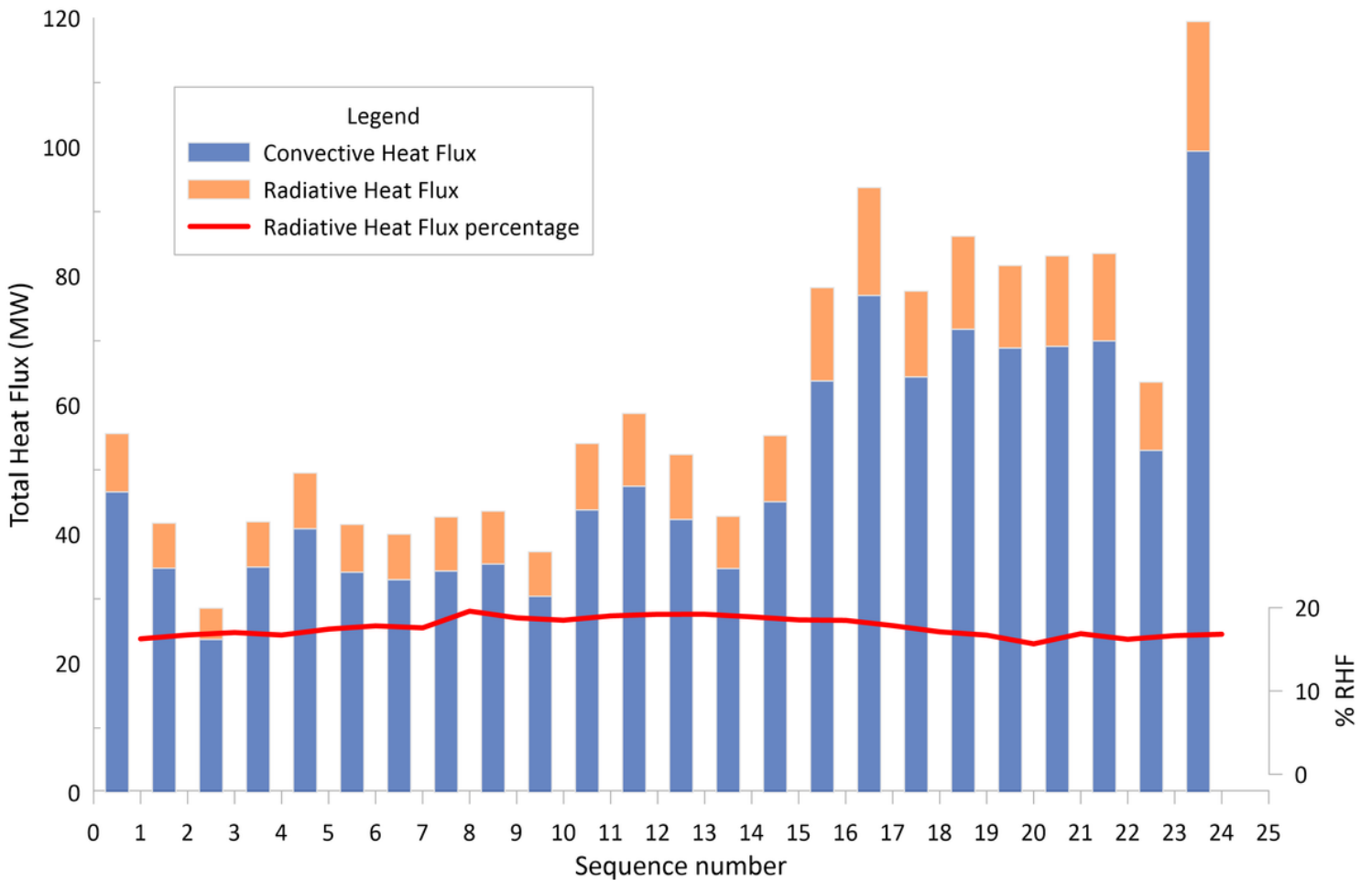The temperature trends recorded in the HTFs on the northern slope of La Fossa

Figure 20

Radiative and convective heat flux partitioning calculated from ASTER

	2021												2022		
	J	F	M	A	M	J	J	A	S	O	N	D	J	F	M
GRAY T$_{15}$	=		=	++	++	++		++	++		++	++		++	
STI	←	low levels	→	+		++	+++	+++		no data		++		++	
MZ1 T$_{15}$	←	no data	→	+				+++	+++		+++				
DDS T$_{15}$	←	no data	→	=				+++	- - -		+		-		
CO$_2$ flux	←	low levels	→	+				+++	++	++	++	++	++	++	++
T2	=		=		=	+	++	+++		=			=		=
T3	+++			+++			+++			+++			++	=	
FA	=		=		=		=		=		=		=		=
FTI		VERY LOW			LOW			HIGH			VERY HIGH				
Profile1 T$_{15}$		LOW			MEDIUM			VERY HIGH			HIGH				
Grid1 T$_{15}$		LOW			MEDIUM			VERY HIGH			HIGH				
VLP	←	very low levels	→					+++	+++		+++			++	++

Figure 21

Summary of unrest onset and behavior depending on the dataset. CO$_2$ flux from the ground continuous data and repeated surveys (Inguaggiato et al., 2022a, 2022b) and VLP events courtesy of INGV (weekly bulletins). Data in italics are from the INGV monitoring network. FTI = Fumarole Thermal Index. HF = Heat Flux. IR = Infrared. STI = Satellite Thermal Index. T2, T3 and FA are monitored HTF. The number of (+) signs gives the magnitude of the increase compared with background levels. The sign (=) means that the signal is stationary. Black rectangles indicate continuous data acquisition as opposed to punctual field campaign data.
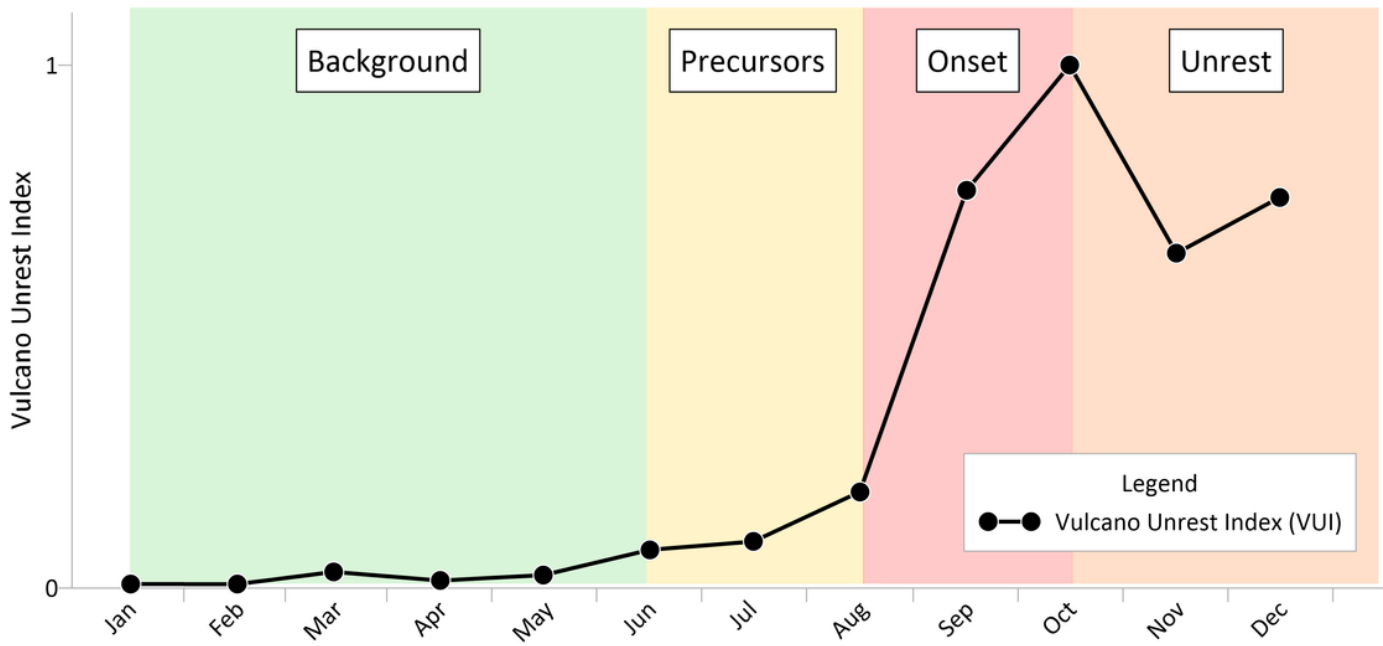
Figure 22

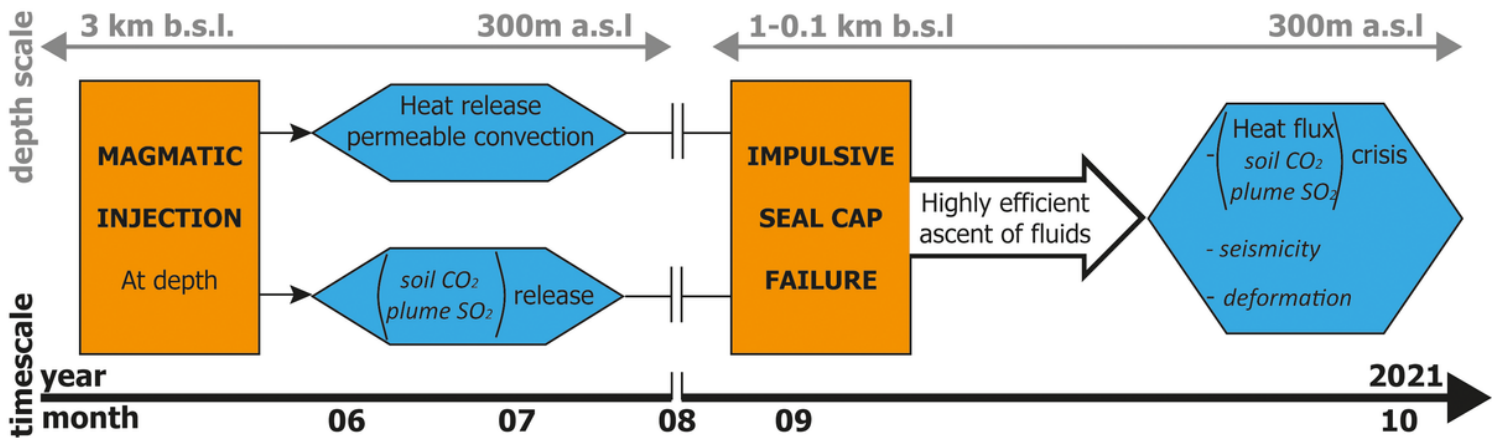Vulcano Unrest Index (VUI) during 2021.

Figure 23

Process system for unrest at Vulcano during 2021, thermally controlled. Time scale is based on the data presented here. Depth for the magmatic system is from Aiuppa et al. (2022) and depth for the hydrothermal system is from (Gambino and Guglielmino, 2008). Parameters in italics are taken from INGV monitoring station data and the first published papers about this unrest (Aiuppa et al., 2022; Inguaggiato et al., 2022a, 2022b).

Supplementary Files

This is a list of supplementary files associated with this preprint. Click to download.

- AppendixBFreqD2.tif
- AppendixC.png
- AppendixD.tif
- AppendixE1.tif
- AppendixE2.tif

- AppendixE3.tif
- AppendixF.tif
- GraphicalAbstract.png
- Preparingadditionalfiles.docx